TECHNISCHE UNIVERSITÄT WIEN
Vienna | Austria

DIPLOMARBEIT

Infrared spectroscopy of Fe_2VAl Heusler compounds

zur Erlangung des akademischen Grades

Diplom-Ingenieurin

im Rahmen des Studiums

Technische Physik

eingereicht von

Sahra Black
Matrikelnummer 01425259

ausgeführt am Institut
der Fakultät für Festkörperphysik der Technischen Universität Wien

Betreuung
Betreuer: Dr.phil. Evan Constable
Betreuer: Dr.rer.nat. Andrei Pimenov

Wien, 07.12.2022

Unterschrift Verfasserin

Unterschrift Betreuer/in

1 Abstract

Heusler compounds are a very broad class of materials first discovered by Friedrich Heusler in 1903. They are intermetallic compounds which show a big variety of physical phenomena, such as superconductivity, shape memory behavior or topological insulators. Some of which are well understood and can be manufactured following specific rules. Additionally, some Heusler compounds have been found to posses a high efficiency for thermoelectric applications which makes them a major research interest.

One of the main quests for thermoelectric applications is the challenge to improve the overall efficiency of the conversion from heat to electricity which is given by the thermoelectric figure of merit (ZT). Several material parameters play a vital role in ZT. Different approaches have been found in order to optimize the various material parameters and therefore maximize ZT. One such approach is approximated in the samples investigated in this thesis. Through the introduction of disorder by thermal quenching or by doping with aluminum an additional peak in the density of states has been predicted by density functional theory simulations. Such a peak near the Fermi energy would enhance the thermoelectirc figure of merit.

This work investigates Heusler compounds based on Fe_2VAl which were either doped with aluminum or quenched at higher temperatures. With the help of a Fourier-transformed infrared (FTIR) spectroscopy the optical reflectivity was recorded at room and low temperatures. Using the Kramers-Kronig relation the optical conductivity was calculated and fitted with a Drude-Lorentz model. The changes in the optical conductivity were analyzed and discussed. Through fitting the data with a Drude-Lorentz model the optical response was separated into different components in order to gain a deeper insight into the thermoelectric transport.

The main finding in this work was the shifting of the interband transition to lower frequencies with higher quenching temperature in the material. Due to the shifting of interband transition in the optical data the pseudogap in the density of states should be decreased with higher quenching temperature. Materials exhibited a relative temperature-

independent optical response which could be beneficial for their applications over the range of the investigated temperatures.

Contents

2 Motivation

Human-induced climate change is one of the most immanent dangers to the world population. Increased weather extremes have reduced food and water security thereby representing a major threat in achieving the Sustainable Development Goals [1]. Increase in food-borne, water-borne, and vector-borne disease are projected with an increased exposure to heatwaves depending on the geographic location. Thereby exacerbating the physical and mental health of people and increase the heat-related mortality globally. This is creating immense economic damages which grow non-linear with raising global warming levels. Adapting and counteracting this catastrophe by diversification in energy production, energy efficiency improvements and many other strategies is of global importance.

Since nearly two-thirds of the energy in industrial applications is wasted as residual heat thermoelectric materials play a vital role into increasing energy efficiency. The automobile industry is a key target for thermoelectric conversion since most heat is lost without recovery. The working temperatures for the processes considered lie in the range of 400 K to 900 K, which is perfect for the application of full and half Heusler materials. Conversion through the use of the Seebeck effect are effective in most regions up to 1.5 °C to 2 °C of global warming levels and the efficiency drops with higher levels.

Fe_2VAl, an iron-based full Heusler alloy is a promising candidate for a green energy conversion and has therefore been studied heavily. Without any moving parts, maintenance is cheap, it is an inexpensive eco-friendly alloy with a long term chemical stability. Additionally it exhibits a relatively large power factor (PF) and thermoelectric figure of merit (ZT) which determine the efficiency of the conversion process. Devices with a ZT value bigger than three would be able to compete with other traditional mechanical power generators. A doped thin film which was based on the studied Heusler compound $Fe_2V_{0.8}W_{0.2}Al$ recently broke the world record for the highest ZT of ~ 5 which has been recorded so far. This shows the clear potential for this alloy [2–6].

Many strategies for improving the efficiency of thermoelectric materials have been studied, such as doping, band engineering or the concept

of phonon like glass crystals. As a purely mathematical question it has been investigated which physical properties should a material possess to be considered the best thermoelectric material. This led to a hypothetical material which would exhibit a Dirac delta distribution at the Fermi energy in its density of states. Since nature does not allow for such distribution to exist two kinds of approximations for this concept implemented in the investigated materials have been studied. One approach was annealing the material at high temperatures and the second one was through aluminum doping of the compound.

3 Theoretical basis

3.1 Boltzmann transport equation

The underlying microscopic theory of electrons in metals can be described by the Boltzmann Transport Equation (BTE), which is a semi-classical theory. It describes the movement of an electron by its probability distribution $f(\mathbf{x}(t), \mathbf{p}(t), t)$ in phase space Ω. Therefore having a specific position $\mathbf{x}(t)$ and momentum $\mathbf{p}(t)$, which violates the Heisenberg uncertainty.

Starting from Newton's law of motion

$$\frac{d\mathbf{x}}{dt} = \mathbf{v} \qquad \text{and} \qquad \frac{d\mathbf{p}}{dt} = \mathbf{F}, \tag{3.1}$$

with $\mathbf{v}$ describing the velocity and $\mathbf{F}$ the external forces. Differentiating the probability density function $f(\mathbf{x}(t), \mathbf{p}(t), t)$ with respect to t yields

$$\frac{df}{dt} = \frac{\partial f}{\partial t} + \dot{\mathbf{x}} \cdot \nabla_{\mathbf{x}} f + \dot{\mathbf{p}} \cdot \nabla_{\mathbf{p}} f. \tag{3.2}$$

The equation above describes the evolution of the non-equilibrium distribution $f(\mathbf{x}(t), \mathbf{p}(t), t)$ in phase space under a force $\mathbf{F}$. Electrons in a solid experience random scattering events which have to be taken into account by adding the expression $(\frac{\partial f}{\partial t})_{sc}$. With no other forces present this yields the full Boltzmann Transport Equation in the following form

$$0 = \frac{\partial f}{\partial t} + \dot{\mathbf{x}} \cdot \nabla_{\mathbf{x}} f + \dot{\mathbf{p}} \cdot \nabla_{\mathbf{p}} f - \left(\frac{\partial f}{\partial t}\right)_{sc}. \tag{3.3}$$

Pursuing a direct solution to Equation 3.3 is extraordinarily difficult with many ingenious techniques developed so far [7]. One difficulty in particular arises from the collision terms $(\frac{\partial f}{\partial t})_{sc}$, which can lead to various complex phenomenon. In many cases the collision term may be treated by the relaxation time approximation, which states that for a small perturbation in the distribution function, f will relax to the equilibrium distribution f_0 on a time scale τ,

$$\left(\frac{\partial f}{\partial t}\right)_{sc} = \left(\frac{f - f_0}{\tau}\right) = \frac{\delta f}{\tau}. \tag{3.4}$$

Here the unperturbed distribution is the Fermi-Dirac distribution in thermal equilibrium $f_0(E) = \frac{1}{exp\left(\frac{E-E_F}{k_B T}\right)+1}$ and the relaxation time τ is the average time between collisions.

3.2 Transport coefficients

The solution of the Boltzmann Transport Equation will give rise to fundamental coefficients in describing thermoelectric transport. A simple derivation shall be given for electrons in a uniform electric field $\mathbf{E}$ pointing in the positive x direction, with the Coulomb force $\mathbf{F} = -e\mathbf{E}$ acting on them. It is assumed that the energy dispersion relation of a free electron is $E = \frac{\hbar^2\mathbf{k}^2}{2m}$, with $\mathbf{k}$ being the wave vector, m being the mass of the electron and $\mathbf{p} = \hbar\mathbf{k}$ holds true. This yields the following relation,

$$\dot{\mathbf{p}} \cdot \nabla_{\mathbf{p}} f = -e\mathbf{E}\mathbf{v}\frac{\partial f}{\partial E}. \tag{3.5}$$

The distribution function f is a function of the reduced energy $\eta = \frac{E-E_f}{k_B T}$ and therefore the following relation holds true,

$$\mathbf{v}\nabla_{\mathbf{x}} f = \mathbf{v}\frac{\partial f}{\partial \eta}\frac{\partial \eta}{\partial T}\frac{\partial T}{\partial x}. \tag{3.6}$$

The difference δf is relatively small compared to the equilibrium distribution f_0 which gives rise to the possibility of inserting f_0 instead of f in the right hand side of Equation 3.2 without introducing huge errors. Yielding the following equation for the transport of electrons,

$$\delta f = \mathbf{v}\tau\frac{\partial f_0}{\partial E}\left(e\mathbf{E}' + \frac{E - E_F}{T}\frac{\partial T}{\partial x}\right), \tag{3.7}$$

with the generalized field $\mathbf{E}' = \mathbf{E} + \frac{\nabla E_F}{e}$.

3.2.1 Electric conductivity

To quantify the flow of carriers in regards to the experienced field $\mathbf{E}'$ the current density $\mathbf{j}$ shall be derived. It depends directly on the charge of the carriers, the number of carriers n and their speed $\mathbf{v}$. With the result above, $\mathbf{j}$ can be expressed as the following,

$$\begin{aligned}\mathbf{j} &= \mp ne\mathbf{v} = \mp e\int_0^\infty g(E)\mathbf{v}(E)[f(E)]dE, \\ &= \mp e\left\{\underbrace{\int_0^\infty g(E)\mathbf{v}(E)[f_0(E)]dE}_{=0\ (stationary)} + \int_0^\infty g(E)\mathbf{v}(E)[f(E)]dE\right\},\end{aligned} \tag{3.8}$$

with $g(E)$ being the density of states and the carrier concentration given by $n = \int_0^\infty g(E)f(E)dE$. For a three dimensional case, the density of states can be expressed as $g(E) = \frac{1}{2\pi^2}\left(\frac{2m}{\hbar^2}\right)^{3/2} E^{1/2}$.

Thus this transforms the Equation 3.8 into the following expression

$$\mathbf{j} = \mp \frac{2e(2m)^{1/2}}{3\pi^2\hbar^3} \int_0^\infty E^{3/2}\tau \frac{\partial f_0}{\partial E} \left(e\mathbf{E}' + \frac{E - E_F}{T} \frac{\partial T}{\partial x} \right) dE, \tag{3.9}$$

where two driving forces contribute to the electrical current. The first term describes the electric flow due to the electric field $\mathbf{E}'$ and the second term is the contribution from a temperature gradient ∇T in the material.

Under isothermal conditions $\nabla T = 0$, Ohm's law $\mathbf{j} = \sigma\mathbf{E}'$ is valid and is used to express the electrical conductivity as follows,

$$\sigma = \mp \int_0^\infty \sigma(E) \frac{\partial f_0}{\partial E} dE, \tag{3.10}$$

with

$$\sigma(E) = \frac{2e^2(2m)^{1/2}}{3\pi^2\hbar^3} E^{3/2}\tau. \tag{3.11}$$

Solving this leads to the electric transport coefficient of

$$\sigma = \frac{2e^2(2m)^{1/2}}{3\pi^2\hbar^3} E_F^{3/2}\tau. \tag{3.12}$$

Using the Fermi energy for a non-interacting spin 1/2 ensemble in three dimension $E_F = \frac{\hbar^2}{2m}(3\pi^2 n)^{2/3}$ the Equation 3.12 can be expressed as

$$\sigma = \frac{ne^2\tau}{m} = ne\mu, \tag{3.13}$$

where μ describes the electron mobility. Equation 3.13 is the same conductivity as predicted by the Drude model for free electrons.

3.2.2 Seebeck coefficient

Assuming that the material is under a temperature gradient $\nabla T \neq 0$ and the circuit is open $\mathbf{j} = 0$ leads to the derivation of the Seebeck coefficient. It describes the conversion of heat into electricity, whereas the opposite conversion is described by the Peltier effect. The Seebeck coefficient is defined by the Equation

$$S = \frac{\mathbf{E}}{\nabla T}. \tag{3.14}$$

Using Equation 3.11 the charge current density can be written in the form,

$$\mathbf{j} = \mp\frac{1}{e}\int_0^\infty \sigma(E)\frac{\partial f_0}{\partial E}\left(e\mathbf{E}' + \frac{E-E_F}{T}\frac{\partial T}{\partial x}\right)dE. \tag{3.15}$$

For integrals involving the equilibrium distribution f_0 the asymptotic formula holds true for $E_F >> k_BT$ and states that, [8]

$$-\int_0^\infty \phi(E)\frac{\partial f_0}{\partial E} = \phi(E_F) + 2\sum_{n=1}^{\infty} c_{2n}(k_BT)^{2n}\frac{d^{2n}\phi(E_F)}{dE_F^{2n}}, \tag{3.16}$$

$$c_{2n} = \sum_{s=1}^{\infty}\frac{(-1)^{s+1}}{s^{2n}}. \tag{3.17}$$

Applying the asymptotic formula to Equation 3.15 up to the second order yields

$$\mathbf{j} = \mp\left[-\frac{1}{e}e\mathbf{E}'\sigma(E_F) - \frac{1}{eT}\frac{\partial T}{\partial x}\frac{\pi^2}{3}(k_BT)^2\frac{\partial\sigma(E)}{\partial E}\bigg|_{E=E_F}\right]. \tag{3.18}$$

From this the Seebeck coefficient can be derived as

$$S = -\frac{\pi^2}{3e}k_B^2T\frac{\partial ln(\sigma(E))}{\partial E}\bigg|_{E=E_F}, \tag{3.19}$$

which is commonly known as the Mott formula.

3.2.3 Electronic thermal conductivity

In a solid thermal energy can be transported by different particles, one of the major contributions in semiconductors are electrons and phonons. Being additive, the total thermal conductivity is given by the electronic and phononic thermal conductivity.

$$\kappa = \kappa_e + \kappa_{ph} \tag{3.20}$$

In order to derive the electronic part of the conductivity the heat current density $\mathbf{q_e}$ transported by the electrons shall be calculated. It depends on the number of electrons, n, times the velocity, $\mathbf{v}$, times the energy transmitted, $(E - E_F)$, which is given by,

$$\begin{aligned}\mathbf{q_e} &= \mp\int_0^\infty \mathbf{v}(E-E_F)f(E)g(E)dE,\\ &= \mp\frac{1}{e^2}\int_0^\infty (E-E_F)\sigma(E)\frac{\partial f_0}{\partial E}\left(e\mathbf{E}' + \frac{E-E_F}{T}\frac{\partial T}{\partial x}\right)dE.\end{aligned} \tag{3.21}$$

From that, the electric thermal conductivity can be expressed as the quotient of the heat current density $\mathbf{q_e}$ to the applied temperature gradient ∇T,

$$\kappa_e = \frac{\mathbf{q_e}}{-\nabla T}. \tag{3.22}$$

This leads to the formula,

$$\kappa_e = \frac{\pi^2 k_B^2 T}{3e^2}\left[T\left(\frac{\partial E_F}{\partial x}\right)\frac{1}{\frac{\partial T}{\partial x}}\left(\frac{\partial \sigma(E)}{\partial E}\right)_{E=E_F} + \sigma\right], \tag{3.23}$$

which can be compactly written as,

$$\kappa_e = L_0 \sigma T - S^2 \sigma T, \tag{3.24}$$

with L_0 being the Lorentz number. It can be noted that for heavily doped semiconductors, the second term can be neglected leading to the Wiedemann-Franz law for semiconductors.

3.2.4 Lattice thermal conductivity

The second major process by which heat energy propagates through solid states are quantized lattice vibration called phonons. Equally as for the electronic thermal conductivity Equation 3.22 holds true. The heat current density $\mathbf{q_{ph}}$ can be described as the sum of the phonon energy times the group velocity of the lattice vibration.

$$\mathbf{q_{ph}} = \sum_{k,p} \hbar\omega f_{ph} \mathbf{v} \tag{3.25}$$

Here the summation is over all wavevectors k and phonon branches. With phonons being bosons, the underlying statistic used is now the Bose-Einstein distribution with the equilibrium distribution being,

$$f_{0,ph} = \frac{1}{exp(\frac{E-E_F}{T}) - 1}. \tag{3.26}$$

Under the condition that external forces do not interact with phonons and the relaxation time approximation can be used, the Boltzmann transport Equation can be written as,

$$f_{ph} = -\tau_c \mathbf{v} \frac{\partial f_{0,ph}}{\partial T}\frac{\partial T}{\partial x}. \tag{3.27}$$

This can be inserted into Equation 3.25 leading to the formula,

$$\mathbf{q_{ph}} = -\sum_{k,p} \hbar\omega\tau_c \mathbf{v}^2 \frac{\partial f_{0,ph}}{\partial T}\frac{\partial T}{\partial x}. \tag{3.28}$$

Utilizing the fact that $\mathbf{v} = v_x\mathbf{x} = \frac{1}{3}v\mathbf{x}$ for a cubic and isotropic system, the thermal phonon conductivity can be written as,

$$\begin{aligned}\kappa_{ph} &= \frac{1}{3}\sum_{k,p} \hbar\omega\tau_c v^2 \frac{\partial f_{0,ph}}{\partial T}, \\ &= \frac{1}{3}\sum_{p} \int_0^{\omega_D} \hbar\omega\tau_c v^2 \frac{\partial f_{0,ph}}{\partial T} g_{ph}(\omega) d\omega,\end{aligned} \tag{3.29}$$

where ω_D is the Debye frequency and $g_{ph}(\omega)$ is the density of states derived from the Debye model. This is called the Klemens-Callaway model, which is a good approximation for the lattice thermal conductivity. However it should be noted that there are a variety of scattering mechanisms for phonons which are not covered by this model [9–13].

3.3 Efficiency of thermoelectric materials

In designing thermoelectric materials, the understanding of their efficiency is one of the most important quantities to optimize, additionally to other properties like cost, toxicity, stability and many more. The simple premise for these materials is to convert heat into electricity or vice versa. To gain a deeper understanding into how efficient these materials can be, a quick derivation based on a thermoelectric generator shall be discussed.

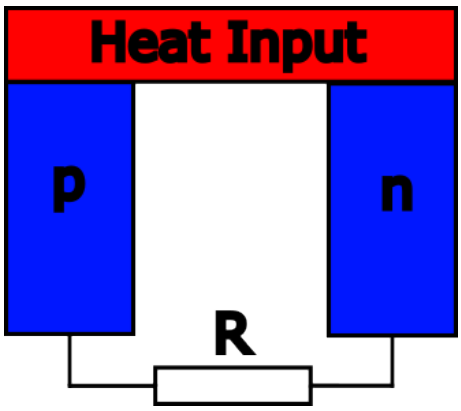

Figure 1: Schematics of a thermoelectric generator converting heat into electricity.

A thermoelectric generator consists of an n-type and p-type conductor, in which the major carriers are either electrons or holes. One side of the system is exposed to a higher temperature than the other side resulting in a temperature gradient. This gradient shall be converted into electricity by electrically closing the system with a resistor, seen in Figure 1.

The efficiency of such a system can be expressed by the amount of power which can be extracted from the system over the introduced amount of power by heat, where the extracted power $P_{e,out} = I^2R$ is determined by Ohm's Law. Applying a temperature gradient to the system results in power, which consist of the Seebeck effect SIT_H, the thermal conductivity $\kappa\Delta T$ and ohmic losses $-\frac{Ir^2}{2}$.

The efficiency can be therefore expressed as,

$$\eta = \frac{P_{e,out}}{\dot{Q}_{in}} = \frac{\Delta T}{T_H} \frac{\frac{m}{(m+1)}}{1 + \frac{\kappa r}{S^2}\frac{m+1}{T_H} - \frac{\Delta T}{2T_H}\frac{1}{m+1}}, \tag{3.30}$$

with r as the internal resistivity of the system, T_H is the high temperature, ΔT is the temperature difference over the system and the quotient $m = \frac{R}{r}$. This illustrates that the efficiency depends on the temperature of the cold and hot junction, the ration m and the quantity $Z = \frac{S^2}{\kappa\rho}$.

The maximum efficiency possible is bounded by the Carnot process and is given by the formula,

$$\eta_{max} = \frac{\Delta T}{T_H} \frac{\sqrt{1 + ZT_M} - 1}{\sqrt{1 + ZT_M} + \frac{T_C}{T_H}}, \tag{3.31}$$

with $T_M = \frac{T_H + T_C}{2}$ [14–16].

For material design, the major quantity describing the maximum efficiency is therefore the dimensionless figure of merit ZT, [4, 17]

$$ZT = \frac{S^2 T}{\kappa\rho}. \tag{3.32}$$

3.3.1 Limitation on ZT

Engineering a good thermoelectric material requires a maximization of the Seebeck coefficient S, while simultaneously minimizing the thermal

conductivity, κ, and the resistivity, ρ. Understanding the theoretical background, it becomes clear that these coefficients are not independent by nature. The hunt for optimized materials are restrained by certain limitations which are inevitable and require careful investigation into the different material properties.

A well known limitation for optimizing ZT is the conflict between the Seebeck coefficient S and the conductivity σ when varying the carrier concentration n. While increasing the carrier concentration leads to a higher conductivity it simultaneously diminishes the Seebeck coefficient. This can be expressed by the Pisarenko relation, which dictates an inverse behavior between the Seebeck coefficient, S, and the carrier concentration, n. It is valid for metals and degenerate semiconductors with parabolic bands [18].

The most important relationships of the parameters are given by the following Equations,

$$S = \frac{8\pi^2 k_B^2}{3eh^2} m^* T \left(\frac{\pi}{3n}\right)^{2/3}, \tag{3.33}$$

$$\sigma = \frac{ne^2\tau}{m} = ne\mu, \tag{3.34}$$

$$\kappa = \kappa_{ph} + L_0 \sigma T, \tag{3.35}$$

where m^* is the density of states effective mass and h is the Planck constant.

From the derivation above it becomes clear that the phonon thermal conductivity, κ_{ph}, is the only parameter which is independent from all others. While this is a good approximation for some materials it is unsurprising that conflicts soon start arising by manipulating κ_{ph}.

Lowering the thermal phonon conductivity κ_{ph} by defects while simultaneous increasing the carrier mobility μ poses therefore another restriction for thermoelectric material design.

Many other connections between parameters can be investigated, which are of great interests for thermoelectric optimization but this is out of the scope of this work [14, 16, 19–22].

3.4 Drude-Lorentz model and optical conductivity

At optical frequencies the Drude-Lorentz model is a good approximation of the electronic behaviour of the investigated samples. Due to the light shone onto the surface of the solid, electrons in the crystal are being accelerated by the electromagnetic force. It can be assumed that the optical response originates from two different types of electrons. First, the free electrons, which are responsible for the metallic response and are described by the Drude model. On the other hand, electrons which are bound to atoms can be polarized in a magnetic field and can be approximated by the Lorentz part of the model.

First, the response of the unbound electrons shall be modeled in an external field **E**. The general equation of motion in a solid can be expressed as,

$$m\ddot{r} + m\Gamma\dot{r} = -e\mathbf{E}, \tag{3.36}$$

where $\Gamma\dot{r}$ is the damping force and $e\mathbf{E}$ is the force experienced by the external field. Here, the damping force represents the average force experienced due to lattice collisions. It is the only force restricting the free flow of electricity in the material.

The solution to Equation 3.36 is given by the Drude model,

$$\epsilon(\omega) = -\frac{\omega_p^2}{\omega^2 + i\frac{\omega}{\tau}}, \tag{3.37}$$

where $\omega_p = \sqrt{\frac{4\pi ne^2}{m}}$ is the plasma frequency and $\tau = \frac{m}{\Gamma}$ is the plasma frequency scattering time. Following Ohm's Law, the conductivity can be expressed as,

$$\sigma(\omega) = \frac{\sigma_{dc}}{1 - i\omega\tau}, \tag{3.38}$$

$$\sigma_{dc} = \frac{ne^2\tau}{m} = \frac{\omega_p^2\tau}{4\pi}. \tag{3.39}$$

The Lorentz model considers electrons bound to atoms in the lattice, which can be polarized in an external electromagnetic field. In the general equation of motion an additional term $\omega_0^2 r$ was added which arises due to the polarization in an external field. This additional

force in the material can be expressed as a harmonic oscillator leading to the following expression,

$$m\ddot{r} + m\Gamma\dot{r} + m\omega_0^2 r = -e\mathbf{E}. \tag{3.40}$$

Solving the system for the bound electrons gives the dielectric function for a Lorentz oscillator as follows,

$$\epsilon(\omega) = \frac{\Delta\epsilon_j\omega_j}{\omega_j^2 - \omega^2 - i\gamma_j\omega}, \tag{3.41}$$

where $\Delta\epsilon_j$ describes the dielectric amplitude of the oscillator, ω_j is the resonance frequency of the oscillator and γ_j is the damping. Although the Lorentzian models predicts the behavior for bound electrons it is also a valid description for IR-active phonons.

The dielectric function for the Drude-Lorentz model yields the following formula,

$$\epsilon(\omega) = \epsilon_\infty - \frac{\omega_p^2}{\omega^2 + i\frac{\omega}{\tau}} + \sum \frac{\Delta\epsilon_j\omega_j}{\omega_j^2 - \omega^2 - i\gamma_j\omega}, \tag{3.42}$$

where the constant ϵ_∞ takes the response of the tightly bound core electrons into account.

The reflectivity for normal-incidence can be therefore calculated with,

$$R(\omega) = \left|\frac{1 - \sqrt{\epsilon(\omega)}}{1 + \sqrt{\epsilon(\omega)}}\right|^2. \tag{3.43}$$

In the low frequency limit it can be shown that the Hagen-Rubens relation,

$$R = 1 - \sqrt{\frac{2\omega}{\pi\sigma_{dc}}}, \tag{3.44}$$

is a valid approximation for metals, where σ_{dc} is the static resistivity. This forms the connection between the resistivity measurements and reflectivity measurements [23].

4 Strategies for improving ZT

Over the years, many approaches for tailoring the properties of thermoelectric materials to maximize the thermoelectric figure of merit ZT have been investigated. Many of them are considered to be state of the art methods of achieving the highest possible conversion coefficient. Since the efficiency is bounded by the parameters in Equation 3.32, great effort has been undertaken into understanding the relationship between them and engineering materials with the desired outcome. A rather incomplete list of important strategies shall be given to demonstrate the underlying concepts and shall be finished with the main approach implemented in the samples investigated in this work.

4.1 Alloying and doping

The process of alloying and doping has been applied for centuries to enhance the desired properties of materials. Utilizing a suitable dopant it is possible to increase the carrier concentration, n, and introduce additional energy levels in between the bands, thereby enhancing the the electrical conductivity σ. As discussed before, this comes at a price of decreasing the Seebeck coefficient S. Furthermore the introduction of disorder in the material has an additional advantage of lowering the thermal phonon conductivity, κ_{ph}, in the material. Due to this trade-off good thermoelectric materials exhibit a carrier concentration in a range of roughly 10^{19} to 10^{21} per cm^3.

4.2 Phonon scattering

One of the broadest investigated approaches are strategies to decrease the thermal phonon conductivity, κ_{ph}, as it is the parameter with the highest independence from other parameters. Therefore a great number of methods have been developed around manipulating κ_{ph} which can be applied simultaneously through a multiscale approach. Here we shall give a little inside into the applied methods concerning this approach.

For a perfect crystal the main scattering mechanism is anharmonic phonon-phonon interactions, which effects the whole frequency range equally. Point defects in a crystal lattice represent additional scat-

tering centers, which lower the phonon thermal conductivity further, these could be for example, vacancies, impurities and dopants. Since they lie on the length scale of phonons they are efficient at scattering phonons and can be introduced in a more or less controlled way into the crystal matrix. Another way to distort the lattice is through the introduction of boundary grains, nano-inclusions or nanostructuring. It should be noted that distortions to the lattice can also effect carrier mobility μ in a negative way.

The concept of Phonon-glass electron-crystal (PGEC) is another investigated method, trying to introduce properties of a glass into the crystal. Crystals posses usually a high electrical conductivity, σ, but also a high thermal conductivity, κ, while glasses exhibit low κ but low Seebeck coefficient, S. This could be achieved by the introduction of phonon rattlers which exhibit a low frequency vibration mode and interact with acoustic phonons. Many other methods exist in trying to maximize phonon scattering [9, 21, 24, 25].

4.3 Singularity in the DOS

Mahan and Sofo investigated the problem of optimizing thermoelectric materials from a mathematical point of view and tried to find the conditions for an ideal thermoelectric [26]. Without assuming any predetermined material properties the transport coefficients have the following general form,

$$\sigma = e^2 \int \left(-\frac{\partial f_0}{\partial E}\right) \Sigma(E), \tag{4.1}$$

$$T\sigma S = e \int \left(-\frac{\partial f_0}{\partial E}\right) \Sigma(E)\,(E-\mu)\,. \tag{4.2}$$

For the highest ZT, their findings showed that the transport function $\Sigma(E)$ should take on the form,

$$\Sigma(E) = \sum_{\mathbf{k}} v_x(\mathbf{k})^2 \tau(\mathbf{k}) \delta(E - E(\mathbf{k})), \tag{4.3}$$

hence showing a Dirac delta distribution in the density of states (DOS). It can be clearly seen that this approach increases the power factor, $PF = S^2\sigma$, directly in the material. A perfect Dirac delta distribution is unachievable in nature. However the investigated samples in this work tried to approximate such a distribution [26].

5 Heusler compund Fe_2VAl

Heusler compounds are intermetallic compounds named after Friedrich Heusler, who studied the first Heusler compound Cu_2MnAl in 1903. They exhibit a broad range of physical phenomena, such as ferro-, antiferro- and ferrimagnetism, semiconductivity, superconductors, shape memory or topological insulator behavior, to name a few. This makes Heusler compounds very attractive to a wide area of applications including thermoelectric conversion [3, 27].

They can be classified into different subgroups, based on their chemical composition. Most important are the full X_2YZ and half Heusler types XYZ, where X and Y are transition elements and Z is a p-Block element. Full Heusler compounds exhibit a $L2_1$ type crystal structure with the space group $Fm\bar{3}m$, which can be seen in Figure 2a.

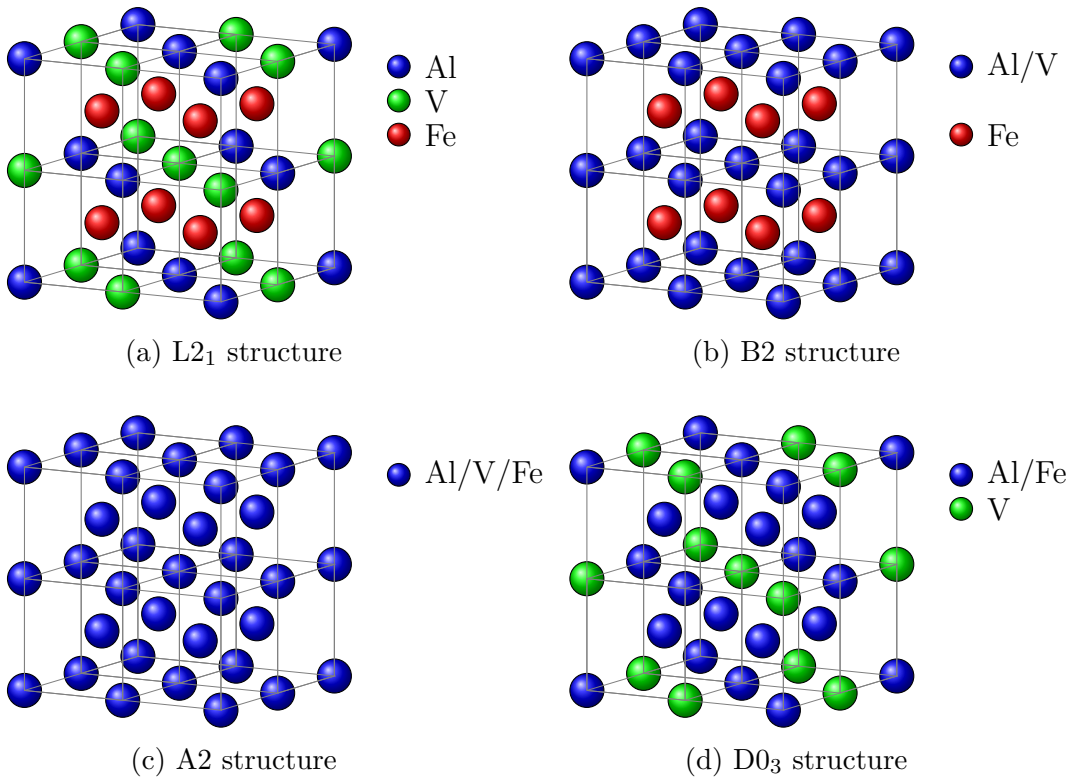

(a) $L2_1$ structure (b) B2 structure

(c) A2 structure (d) $D0_3$ structure

Figure 2: Illustrations of the different crystal structures of the Fe_2VAl Heusler compound.

Iron-based full Heusler alloys Fe_2YZ are a promising candidate for thermoelectric conversion, due to their relatively large PF and ZT,

being eco-friendly inexpensive materials and for their chemical stability [6].

In this work the alloy Fe_2VAl was investigated, which can be described as a semimetal exhibiting a sharp pseudogap of 0.01 eV at the Fermi level. Due to this sharp slope in the density of states the stoichiometric compound exhibits a high Seebeck coefficient $S \approx 70\ \mu V/K$ at 300 K. With a measured resistivity of $\sim 900\ \mu\Omega cm$ and a thermal conductivity of $\sim 28\ Wm^{-1}K^{-1}$ at room temperature, the maximum reached ZT values lie beyond one.

Through thermal quenching with high temperatures (950 - 1350 °C) it was shown that atomic defects could be introduced into the material. Changing the crystal structure from $L2_1$ to a partly disordered B2 to a fully disordered A2 structure with increasing quenching temperatures, seen in Figure 2. By ultrafast quenching the lattice disorder could be partly frozen in the material, thereby controlling the amount of disorder in the sample. Density functional theory calculations showed an emerging sharp hydrogen impurity state near the Fermi energy which improves the thermoelectric transport properties. Thereby, a high power factor, PF, of 18 mW/mK^2 at 400 K has been achieved, a factor 30 times bigger than before and possible ZT values greater than nine, $ZT > 9$, are predicted to be achieved if $\kappa_{ph} = 2.3\ Wm^{-1}K^{-1}$.

The second method for approaching a Dirac delta distribution near the Fermi energy was achieved by doping Fe_2VAl with aluminum. With a rising aluminum concentration the amount of antisite disorders increases altering the crystal structure. The growing off-stoichiometry leads to the appearance of Al antisites on the Fe and V site. Performed density function theory calculations show an increased resonant state appearing at the Fermi energy with increased aluminum concentration. This sharp rise is beneficial for the Seebeck coefficient and led to an increased thermoelectric effect. A Seebeck coefficient of 150 $\mu V/K$ could be observed and a maximum ZT value of ~ 0.15 for $Fe_2VAl_{1.6}$ at around 400 K was achieved, which is one of the highest measured ZT values without optimizing the material further.

An additional effect in both materials was the reduction of the thermal phonon conductivity, κ_{ph}, due to the disorder into the lattice

system [28–30].

6 Method

6.1 Experimental setup

All measurements were carried out with a Bruker VERTEX 80v, a Fourier-transform infrared (FTIR) spectrometer. It is composed of light sources, beamsplitters, a sample chamber and detectors. The spectrometer could be operated under a vacuum of roughly 200 Pa to avoid disturbances from the residual absorption of water molecules. Due to the limited measurement range of the optical elements, various elements had to be utilized to record a full broadband response. Table 1 gives an overview of the elements used in this work. Measurements at room temperatures were carried out by using a plastic plate with a hole as a mount for the samples. The plate was masked using a SiC layer to disperse the light not incident on the sample.

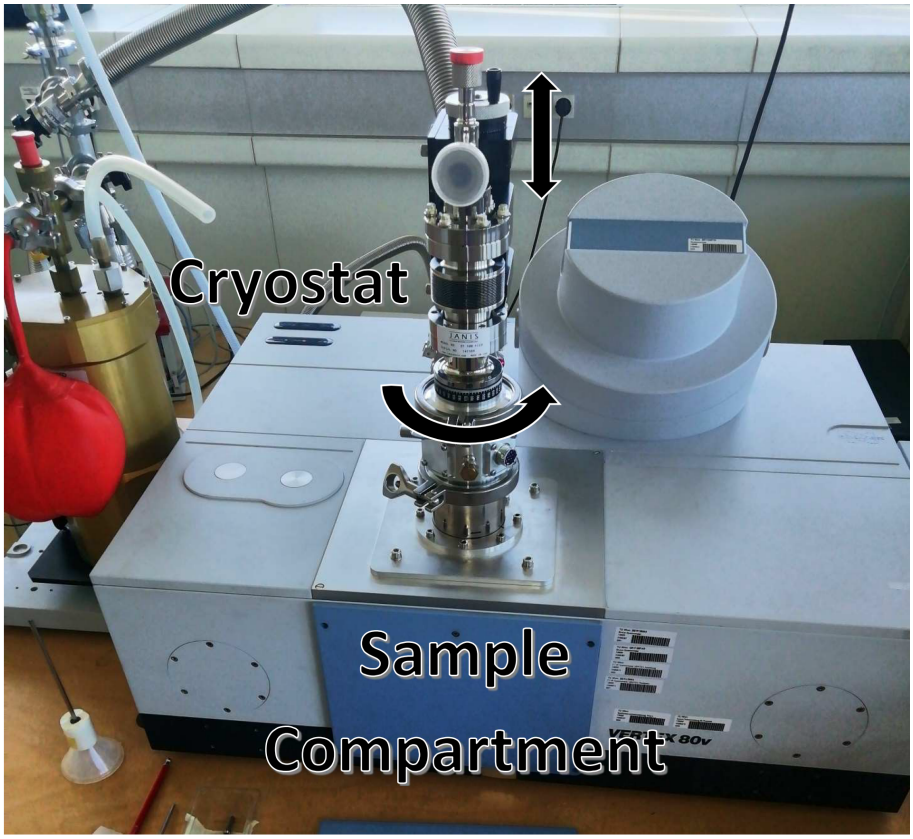

Figure 3: Picture of Bruker VERTEX 80v with the cryostat inserted.

In Figure 3 the setup is depicted with a bolometer on the left side and the inserted cryostat with its degrees of freedom (height and rotation). With the utilization of a helium flow cryostat it was possible to cool the samples down to 4 K and record the temperature dependent reflectivity. The cryostat was evacuated to the high vacuum regime and was equipped with different kinds of windows which were transparent in the investigated frequency range. To ensure a good heat transfer onto the samples, copper plates with three holes were manufactured for the mounting system.

setting	spectral range [cm^{-1}]	source	beamsplitter	detector	window
NIR	8300 - 15000	tungsten lamp	CaF_2	silicon diode	glas
NMIR	4000 - 8300	tungsten lamp	CaF_2	MCT	KBr
MIR	600 - 4000	glowbar	KBr	MCT	KBr
FIR	50 - 600	mercury lamp	Mylar 6 μm	bolometer	polypropylene

Table 1: Settings used to measure the broadband response of the samples.

A gold mirror was used as a reference as it possesses a reflectivity of close to unity over a the investigated frequency range. The recorded intensity was thereby gauged by dividing it by the intensity of the reference which gives the true value for the reflectivity of the sample. A small reflectivity angle of 11°, near-normal incident, allows the Equation 3.43 to be used in analyzing the data.

6.1.1 Optical path

A quick broadband sampling was achieved with the heart of the spectrometer being a Michelson interferometer. In Figure 4 the basic beam path of the spectroscope is laid out. The source emits a beam of light in a characteristic frequency range depending on the source used. This beam gets collimated and the beam width meeting the surface of the sample was adjusted through an aperture.

Next, the beam enters the Michelson interferometer which consists of a beamsplitter, a moving and stationary mirror. Light was separated into two orthogonal beams by propagating through the beamsplitter. On both ends of the path the beam gets reflected by the mirrors and merges at the beamsplitter into one beam. Differences in the optical path length δ of the two channels create interference in the intensity

of the beam. The beam is diverted onto the surface sample in a small angle with the use of additional mirrors. A detector then records the interferogram from the near-normal reflection of the sample.

By moving the mirror position and recording the intensity as a function of the path difference $I(\delta)$ an interferogram is generated from the sample. For a mirror moving at constant speed the changes in the intensity of $I(\delta)$ can be describes as,

$$I(\delta) = \int_{-\infty}^{\infty} I(\nu) cos(2\pi\nu\delta) d\nu, \tag{6.1}$$

with $I(\nu)$ being the intensity from the light source and ν is the frequency. To retrieve the intensity in the frequency domain from the interferogram a Fourier transformation was performed [31, 32].

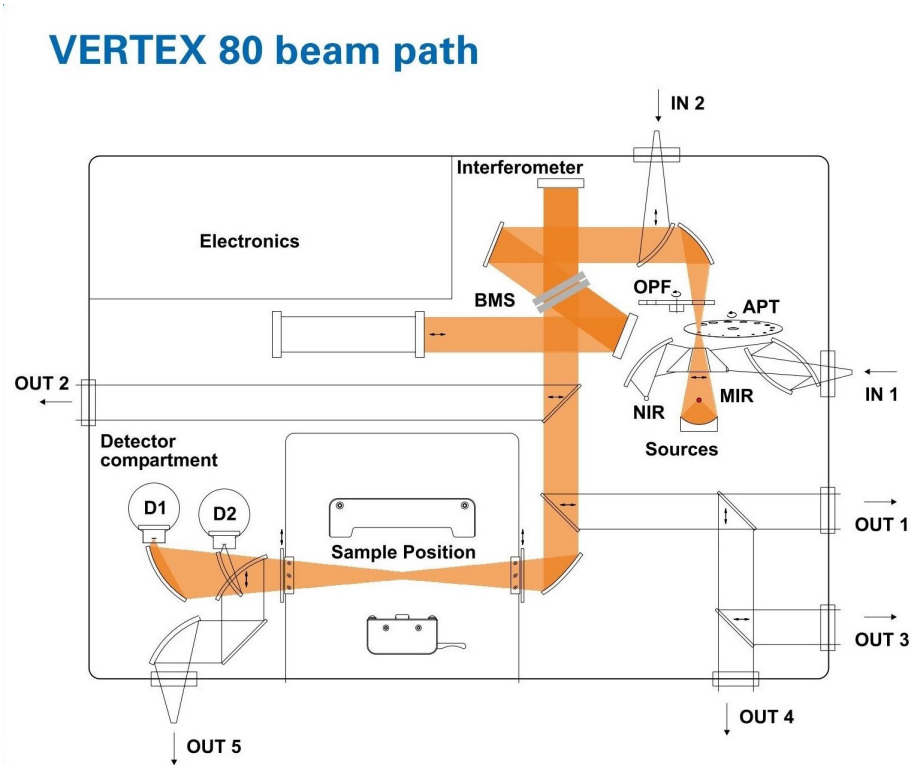

Figure 4: The beam path of Bruker VERTEX 80v from [33].

6.1.2 Issues with the system

During the measurement process multiple issues arose with the current setup which were attempted to be fixed. Here certain issues which were encountered shall be discussed for a better understanding of the

limitations in the recorded data.

Since the probed samples displayed a high reflectivity which was close to the reflectivity of the reference in certain frequencies, accurate values were achieved by a statistical approach. Therefore multiple measurements in different frequency domains were performed, averaged and compared with each other.

One sensitivity investigated was the deviation of the beam path for different elements or by switching the sample. Changing the optical elements such as aperture, source, beamsplitter and others could shift and distort the light beam at the sample surface. Therefore creating an misalignment which had to be realigned.

For small samples sizes in the order of 5 mm the aperture size was another key limitation for measurements. Especially in the far-infrared domain, the correct recording of the low frequencies was an issue.

The sample in the cryostat were mounted on various copper plates with three holes which were in turn mounted to the cryostat with screws. Copper was used due to its high thermal conductivity making it a perfect material of choice for low temperature measurements. Performed measurements showed a change in the intensity for different holes on the same copper plate while mounting gold mirrors. The copper plates were studied further to find a suitable position for the sample and the mirror. Additionally, the measurements were corrected with the help of the room temperature reference where no copper mount was used.

In the low temperature range, below 40 K, an oscillation over time occurred which could be seen in the reflectivity. Cooling the sample down from room temperature to $\sim$ 4 K and starting to capture the temperature dependent reflectivity at 10, 20, 30 and 40 K showed a sudden shift in the reflectivity at 40 K. While staying at temperatures below 40 K revealed a slow oscillation over time in the spectra. This could originate from the cryostat being in non thermal equilibrium and could not be solved in this work. Further study is needed to resolve this issue.

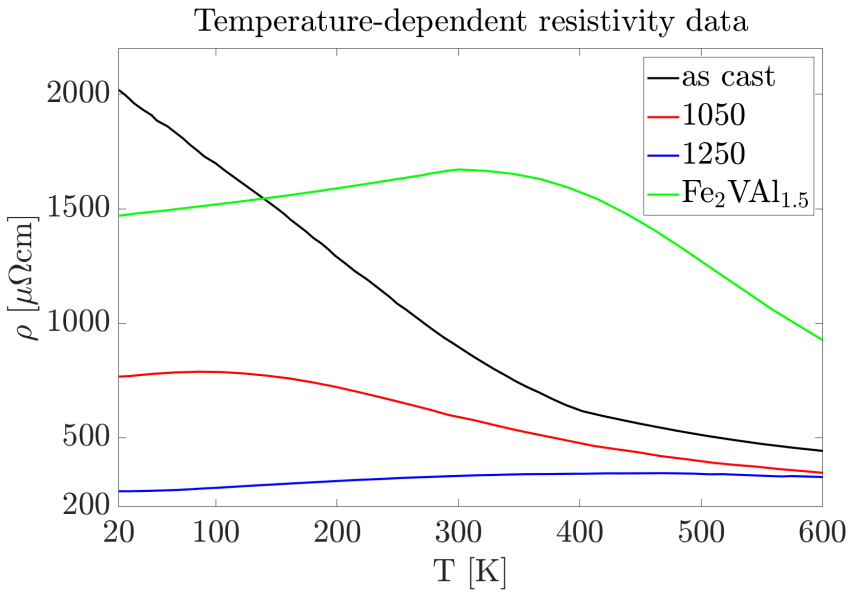

Figure 5: Depiction of the temperature-dependent resistivity data of the samples from [29, 30].

The samples are based on the Heusler compound Fe_2VAl which were either thermally quenched or doped with aluminum. All of the samples are polycrystalline and have been polished to a degree were their surfaces are flat and sufficiently reflective. Samples had different sizes with the smallest surface measuring $\sim$ 2.2 mm in width. Overall four different samples have been investigated which are called Fe_2VAl as cast (as cast), Fe_2VAl 1050 (1050), Fe_2VAl 1250 (1250) and $Fe_2VAl_{1.48}$. In Figure 6 the different samples can be seen as well as the copper plates which were utilized as a mount in the cryostat.

While the as cast sample was cooled down in the furnace directly during manufacturing, the samples 1050 and 1250 were additionally annealed at 1050 °C and 1250 °C for 24h and then rapidly quenched in cold water. $Fe_2VAl_{1.48}$ was doped with aluminum and also cooled down in the furnace.

The temperature dependence of the electrical resistivity of the samples can be seen in Figure 5. It can be noted that quenching the samples at higher temperatures induces a semiconductor to metal transition in the resistivity. Resistivity measurements were used to scale the reflectivity data. The resistivity measurement of the sample $Fe_2VAl_{1.48}$ was not available, therefore the data from the sample $Fe_2VAl_{1.5}$ was

taken instead.

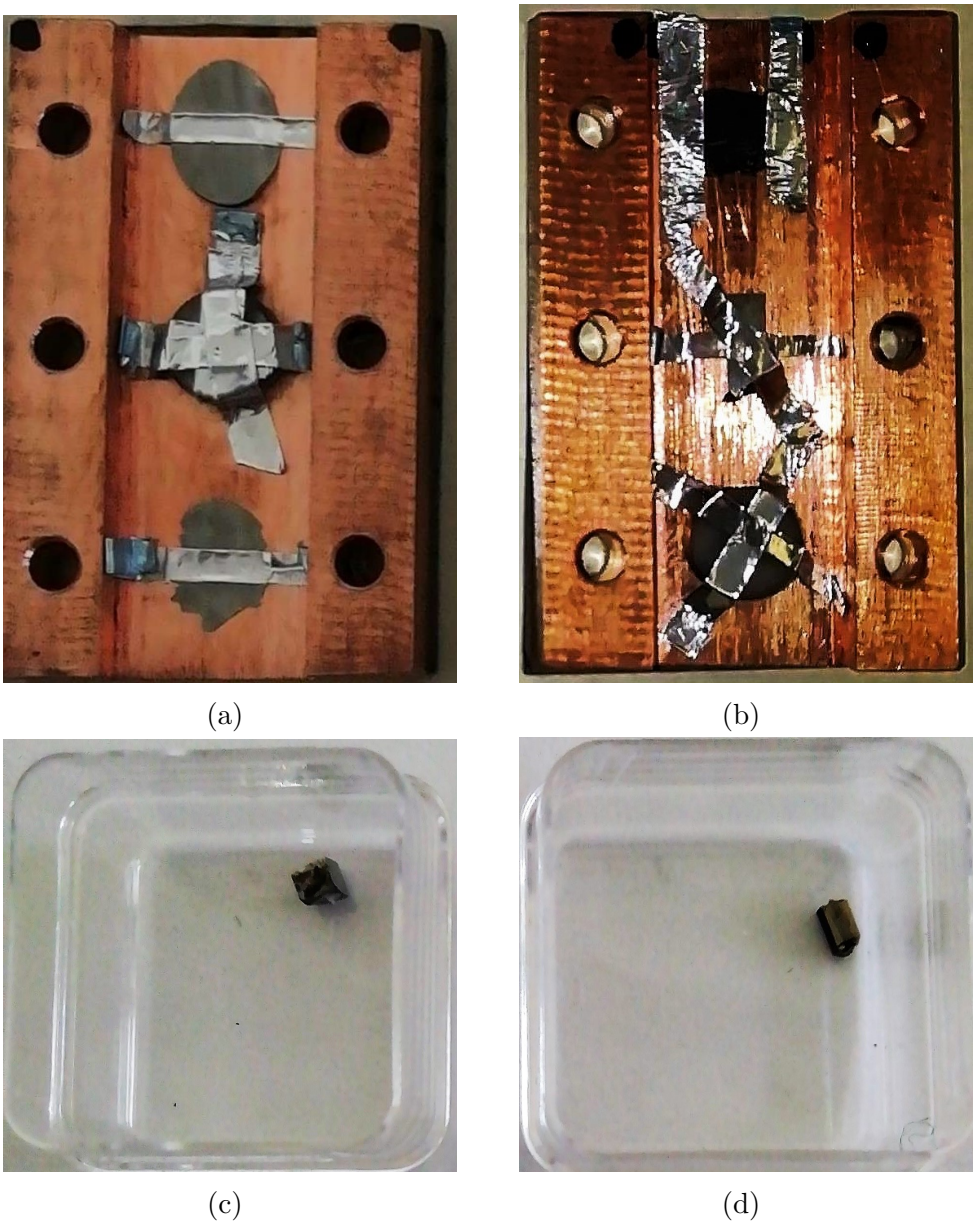

Figure 6: (a) Photo of the copper plate with the mounted gold mirror in the middle position and the sample as cast at the bottom. (b) Copper plate with the samples as cast and $Fe_2VAl_{1.48}$ and the reference mounted from top to bottom. Depiction of the sample (c) 1050 and (d) 1250.

6.2 Data preparation

The reflectivity of the polished Fe_2VAl polycrystal were recorded several times in each optical region and averaged to ensure that the data is reproducible. The full broadband reflectivity was constructed by

stitching the responses in the various domains together. Between domains the reflectivity exhibited an offset due to misalignment of different optical elements. Additionally the data from the cryostat showed an additional offset and some artifacts, which were corrected.

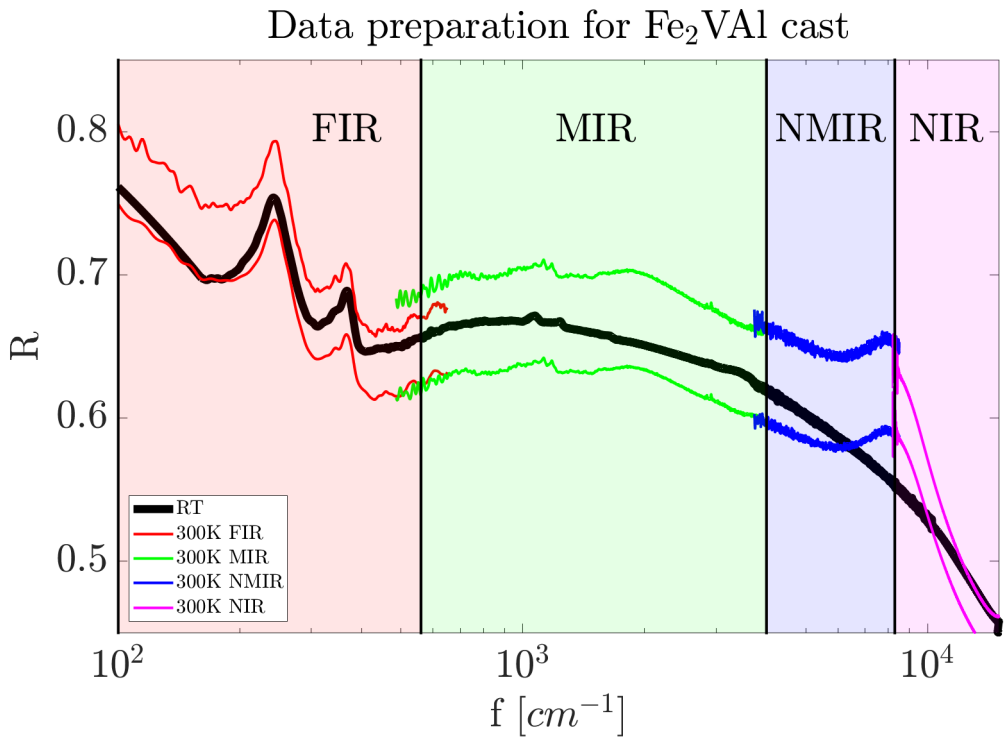

Figure 7: Raw spectra of Fe_2VAl at 300 K in the different optical regions.

For a standardized approach of constructing the final broadband reflectivity, a Hagen-Rubens extrapolation in the low frequency region was chosen as the scaling point at at the frequency f_{cutoff}. With the published temperature-dependent resistivity it was possible to calculate the extrapolation according to Equation 3.44. In the case of the 1250 °C annealed sample the cutoff frequency was chosen to be 210 cm^{-1} and for the rest of the samples f_{cutoff} was 160 cm^{-1}. As a high frequency extrapolation the function $1/f$ was used for frequencies greater than 15000 cm^{-1}. Between different domains, the signal was scaled such that they would overlap at the boundaries. For a smooth transition the stitching point between two domains was appropriately chosen and additionally smoothly fit. Lastly, visible deviations between the measurements with and without the cryostat were removed by scaling the data according to the measurements performed without the cryostat [23, 29, 30].

Figure 7 depicts the recorded optical reflectivity for the sample Fe_2VAl as cast at 300 K. The curves above represent the raw measured data in the different domains. Below them, the black curve displays the measurement at room temperature RT outside the cryostat, which was already scaled according to the corresponding Hagen-Rubens extrapolation. The curves were shifted in such a way that it corresponded with the Hagen-Rubens relation at the cutoff point f_{cutoff}. Thereby demonstrating a good overlap between different optical domains.

Comparing the room temperature, RT (with cryostat), to the 300 K measurement (without cryostat) illustrates the deviations introduced by the cryostat. The deviation in the NMIR and NIR data in the cryostat data stems from an optical misalignment in the setup, which was corrected in the process of data preparation.

6.3 Analysis

To analyze the reflectivity further, a Drude-Lorentz fit was performed following Equation 3.42. Thereby, decomposing the recorded optical response into the different contributions: a Drude, a phononic and an interband part. This was very successful for the as cast and 1050 °C samples. However the fits for the rest of the samples deviated in some parts of the response, which made them hard to compare. As of this reason only the fits for the as cast and 1050 °C samples in the low temperature region were analyzed further.

Furthermore, the response was also investigated through the use of the Kramers-Kronig transformation. For this, an algorithm from literature was programmed in Matlab in order to calculate the dielectric function $\epsilon(\omega)$ and the optical conductivity σ_{opt} [34].

6.4 Reflectivity measurements at room temperature

The measured broadband reflection of the samples is depicted in Figure 8. It is easily recognized, that the as cast sample demonstrates a decreased reflectivity compared to samples treated with higher annealing temperatures. Higher annealing temperatures seems to correspond with higher reflectivity in the compound. However all three samples exhibit a very metallic response to light, which is to be expected from

a semimetal. Doping with aluminum on the other hand seems to decrease the reflectivity. This can be also seen in the calculated optical conductivity, seen in Figure 9 (a,b).

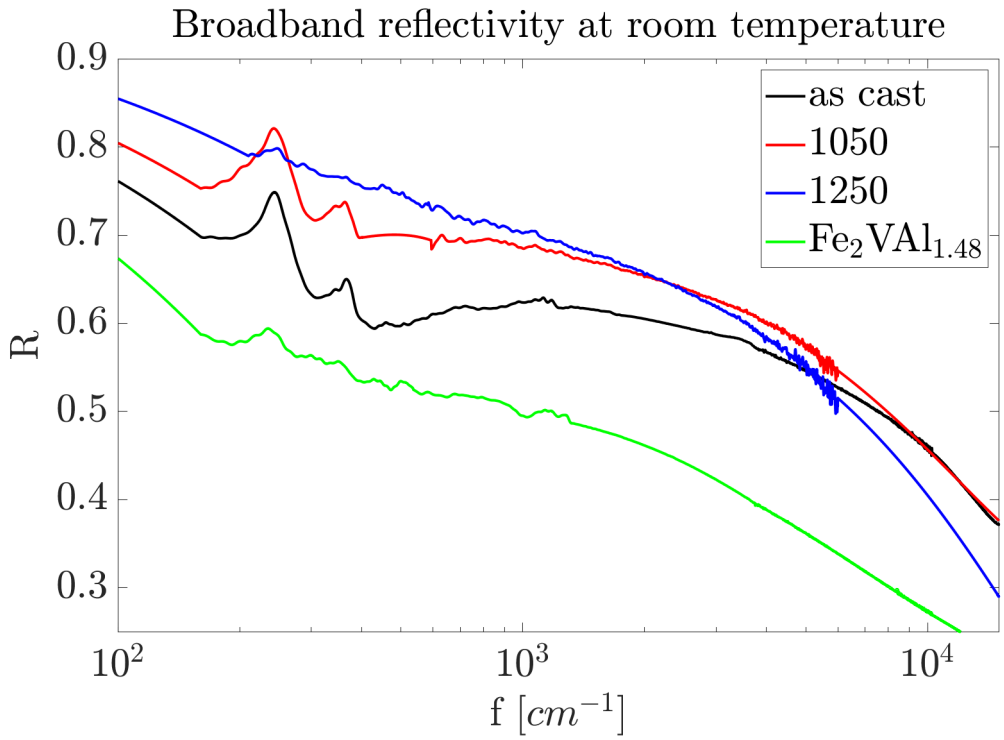

Figure 8: Broadband spectra of the measured samples at room temperature in the cryostat.

In Table 2 the fitting parameters are plotted for the samples at room temperature. With higher annealing temperatures the plasma frequency scattering time, τ, decreases, while the plasma frequency, ω_p, increases. For higher annealed materials the main contribution to the increased reflectivity originates from the higher plasma frequency, which shifts the reflectivity drop-off to higher frequencies. This can be understood from the conductivity of the Drude model in Equation 3.39, where the plasma frequency, ω_p, contributes quadratically to the optical conductivity, σ_{opt}. Thereby enhancing the Drude response in the material. On the other hand the reduced scattering time results in a lower observed reflectivity due to more damping.

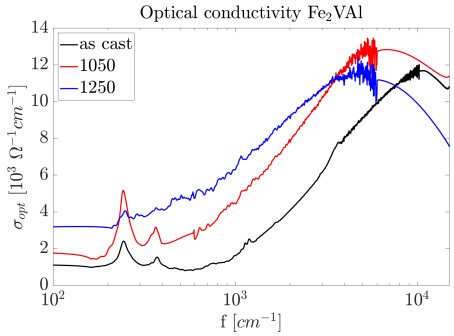

(a) Optical Conductivity

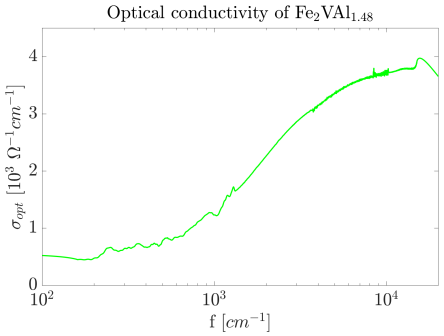

(b) Optical Conductivity of the aluminum doped sample.

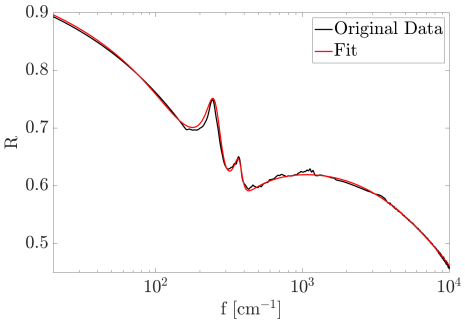

(c) Fit for the sample Fe_2VAl as cast at 300 K.

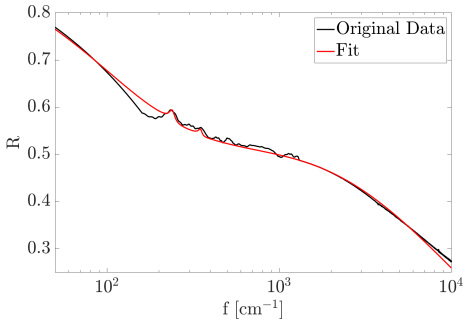

(d) Fit for the sample $Fe_2VAl_{1.48}$ at 300 K.

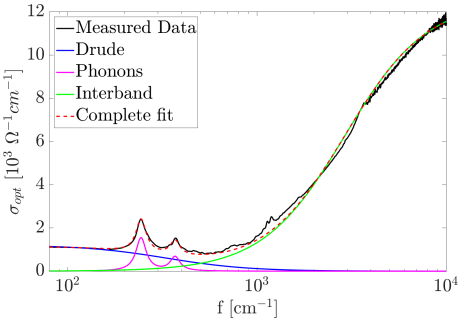

(e) Drawing of the different components of the Drude Loretz model.

Figure 9: Depictions of the optical conductivity and the fitted data overlapped by the original data.

As discussed previously, Fe_2VAl Heusler compounds crystallize into the space group $Fm\bar{3}m$, which has two IR-active phonons. The as cast and 1050 °C samples demonstrate two phonons at roughly 240 cm^{-1} and 360 cm^{-1}. While the sample treated with the highest temperature of 1250 °C and the aluminum doped sample exhibit two attenuated phonons at roughly the same positions [35, 36].

Annealing the compound at higher temperatures seems to initially

harden the phonon modes only to soften them again. This can be easily observed in the plot of the optical conductivity. Fitting the data illustrates that the amplitude for the first phonon $\Delta\epsilon_1$ grows initially and shrinks again with higher annealing temperatures, while the phonon damping, γ_1, decreases. Note, that for the second phonon the damping, γ_2, decreases in a similar fashion, which would indicate that the phonon life time increases. A increased phonon life time $\tau = 1/\gamma$ could point to a increase in the thermal phonon conductivity, κ_{ph}. However the thermal phonon conductivity was decreased in the compounds treated with higher temperatures. Since the phonons were probed by light the elevated optical conductivity could be responsible for the screening of the phonon modes and could therefore explain the observed effect in the compound. It can be noted that annealing seems to improve the coherence of the phonons, however this does not seem to contribute to the increasing κ_{ph} [29].

Fitting parameter	Fe_2VAl cast	Fe_2VAl 1050	Fe_2VAl 1250	$Fe_2VAl_{1.48}$
ϵ_∞	1	1	1	1
ω_p [10^3 cm^{-1}]	2.05	2.87	150.00	2.83
τ [10^{-3} cm]	3.41	2.68	0.0016	0.82
$\Delta\epsilon_1$	17.00	22.70	1.01	0.50
ω_1 [cm^{-1}]	244.00	243.10	246.58	239.80
γ_1 [cm^{-1}]	51.00	32.82	8.52	20.51
$\Delta\epsilon_2$	3.16	3.15	-	0.16
ω_2 [cm^{-1}]	369.40	360.50	-	350.00
γ_2 [cm^{-1}]	53.76	32.21	-	20.00
$\Delta\epsilon_3$	76.67	144.90	134.55	34.00
ω_3 [10^5 cm^{-1}]	1.20	1.45	0.22	0.85
γ_3 [10^6 cm^{-1}]	6.60	20.00	0.93	4.70
n [10^{20} cm^{-3}]	0.49	0.98	1.05	0.952

Table 2: Fitting parameter of the Drude-Lorentz model for the room temperature measurements.

Aluminum doping seems to decrease both the phonon amplitude $\Delta\epsilon$ and the phonon damping γ. Decreasing the phonon damping could increase the thermal phonon conductivity, κ_{ph}. However the thermal conductivity was reduced in the compound by further Al-doping by inducing disorder. Since the optical conductivity, σ_{opt}, is reduced, phonon screening should not contribute to soften the phonon modes.

It should be noted that optical phonons do not contribute much to the thermal phonon conductivity [30].

Lastly it can be noted that the phonon frequency is shifted towards smaller frequencies for the the annealing temperature of 1050 °C and for the Al-doped compound.

One of the main findings in this work is the behaviour of the interband transition and the decline of the pseudogap. The interband response increases and decreases again in their intensity with rising annealing temperatures, which is also observed in the fit of the interband amplitude $\Delta\epsilon_3$. A shift towards lower frequencies for higher annealing temperatures in the broad interband transition can also be confirmed by the measured data. This could not be shown in the fitted data due to the uncertainties near the measurement range. As previously discussed Fe_2VAl exhibits a sharp pseudogap which can be seen in the optical conductivity. The depletion in between the phonons and the onset of the interband transition marks the pseudogap. With rising disorder through annealing or Al-doping the sharp pseudogap visibly declines.

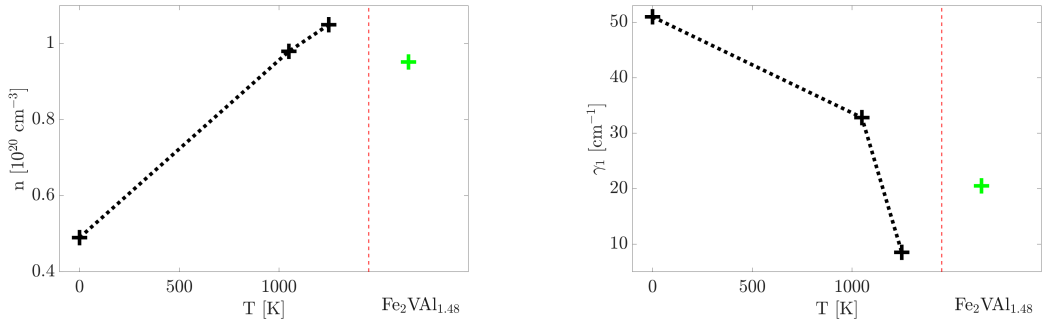

(a) (b)

Figure 10: Plot of the carrier concentration n (a) and the damping of the first phonon γ_1 (b).

Besides these above mentioned phonons the sample Fe_2VAl as cast and $Fe_2VAl_{1.48}$ have two additional phonon-like structures at roughly 1070 cm^{-1} and 1240 cm^{-1}. Since the Heusler compound Fe_2VAl is prone to anti-site disorder other crystal structures can occur in this compound, which could lead to further IR-active phonons appearing.

It is however unclear if this structures are part of the interband transition or if they are optical phonons. It can be also noted that the cryostat distorts these artifacts.

With the use of the fitted plasma frequency the carrier densities were calculated which are plotted in Figure 10 (a). With rising disorder in the lattice system the carrier concentration seems to rise. The Hall carrier density at 300 K for the as cast sample was determined to be $\sim 3 \times 10^{20}$ cm^{-3} which deviates from the calculated concentration of 0.49×10^{20} cm^{-3}. The misalignment in the measured Hall carrier concentration is even bigger for the 1250 sample as the measurement determined $n_H \sim 100 \times 10^{20}$ cm^{-3} compared to the calculated $\sim 1 \times 10^{20}$ cm^{-3} in this work. It should be noted that the major carrier type switches from electrons to holes with higher quenching temperatures as it is indicated by the published Seebeck measurements [29].

6.5 Reflectivity measurements at low temperature

Next the temperature dependency of the samples optical conductivity was analyzed in the hope of gaining new insights into the material.

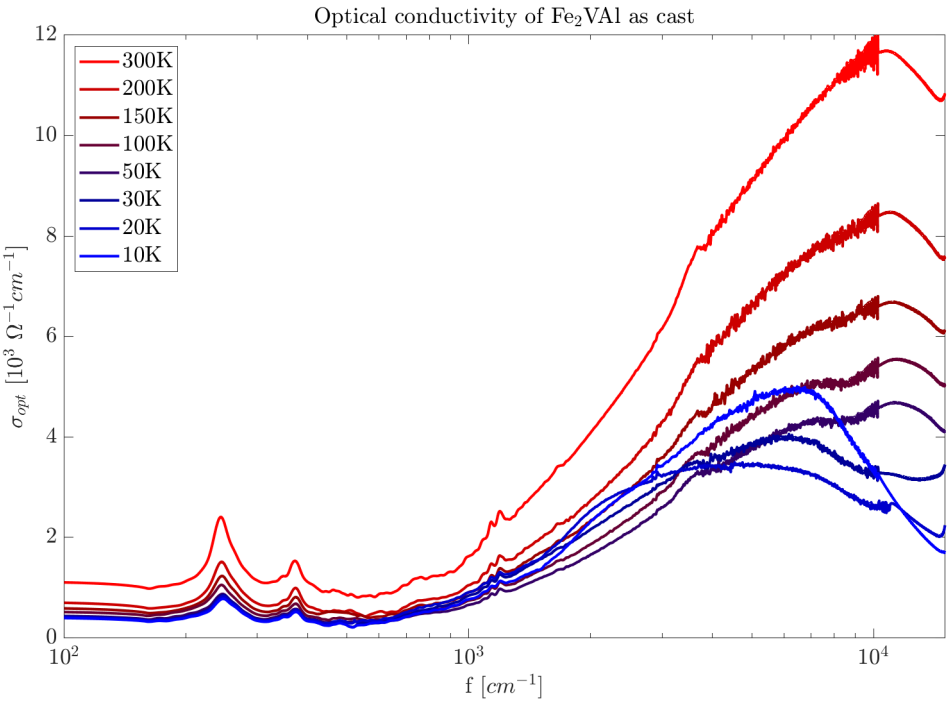

Figure 11: Optical Conductivity of Fe_2VAl cast.

As cast showed the most variation in its response function over the studied temperature range. It can be easily seen that the optical conductivity and thereby the reflectivity is decreasing with lower temperatures. From the fitting parameters of the model in Figure 12 it is clear that the plasma frequency scattering time, τ, tends to increase with lower sample temperature while the plasma frequency, ω_p, decreases. While an increase in τ would point to a increase in the optical conductivity, the decrease in ω_p would have the adverse effect. The observed decrease would indicate a manifestation of the second effect.

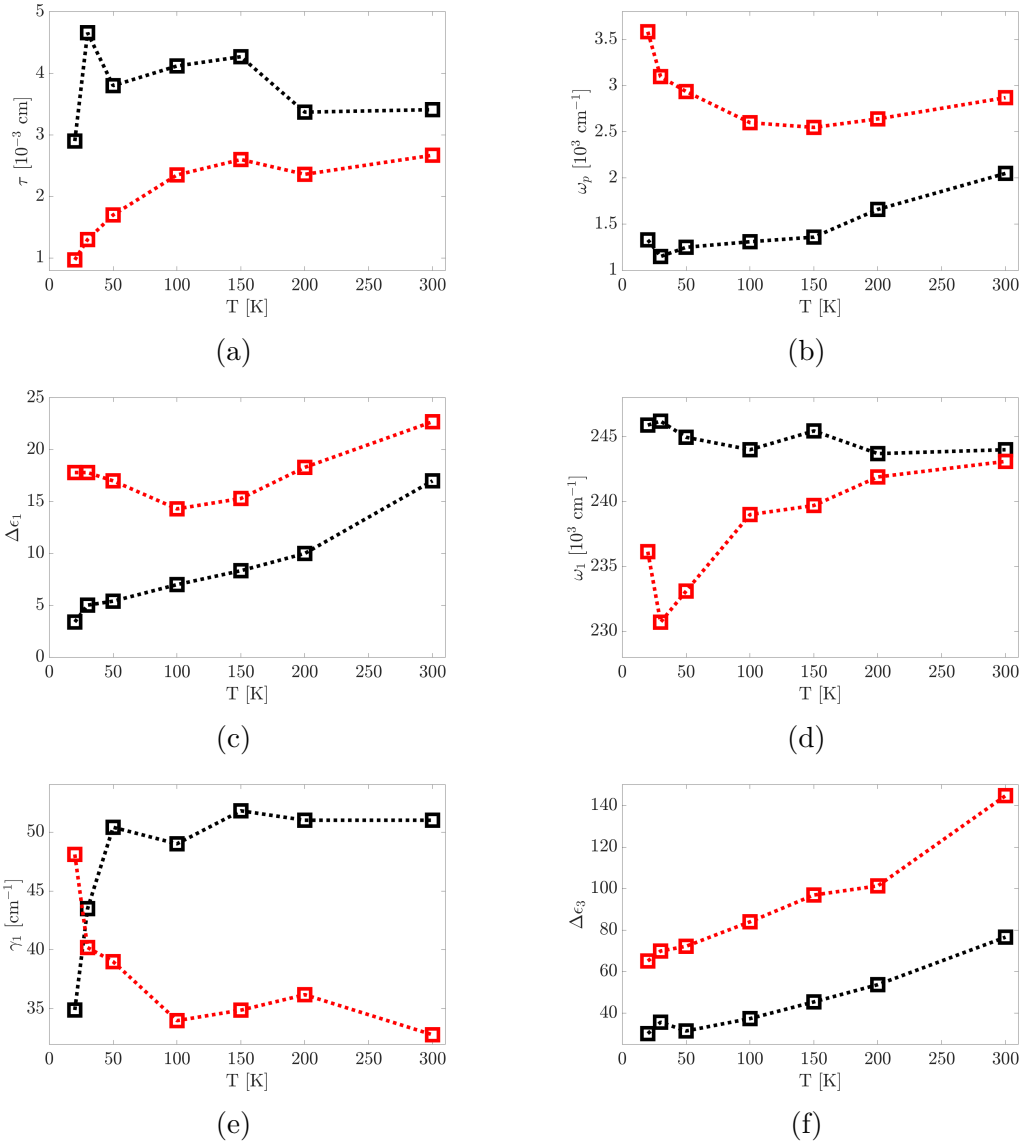

Figure 12: Fitting Parameters at different temperatures. The black cross represents the as cast sample and the red cross depicts the 1050 °C annealed Heusler compound.

Both phonon modes soften with decreasing temperature, which is a very unusual behaviour for semimetals. $\Delta\epsilon_1$ decreases while the damping γ_1 and the phonon frequency ω_1 stays roughly the same. This could also hint at a lattice instability or at the presence of electron-phonon interactions.

The interband transition seems to have a more complex temperature trend. As can be seen by the optical conductivity data from as cast, the interband transitions seems to get stronger with higher sample temperature. From the fits it can also be observed that $\Delta\epsilon_3$ decreases with lower temperatures. A slight shifting of the interband transition to higher frequencies can be observed for lower temperature for T $\geq$ 50 K. While for smaller temperature the maximum of the interband response is moving to smaller frequencies. However the arising issue of the misalignment below temperatures of 40 K could not be solved in this work. Therefore, the shifting of the interband maximum towards smaller frequencies and the overall interband intensity for T $<$ 50K might be incorrect.

The measured data suggests that the pseudogap is relatively independent from the sample temperature with a major jump in the optical conductivity between the 300 K and 200 K data.

From literature measurements of the Fe_2VAl sample it can be noted that the optical conductivity also grows with higher temperatures for the intraband transition. While the interband transition shows an increased response and a shift of the maximum value to lower frequencies with higher sample temperature. However the amplitude of the phonon is independent of the temperature. Also the level of depletion in the optical conductivity of the pseudogap was confirmed to be independent of the sample temperature and therefore constant.

In this work the interband response had a higher optical conductivity measured than in the literature, which could be explained by the variation in the sample manufacturing process. The decline in the phonon modes suggests an error in the measurement of the observed phonons. Since the overall scaling was performed by the Hagen-Rubens relation based on resistivity data the deviation in the optical conductivity from the literature indicates that the cutoff frequency f_{cutoff} was chosen to

be too high or the model is not adequate for this material. Overall the optical conductivity at zero frequency $\sigma_{opt}(\omega = 0) \approx 10^3\ \Omega^{-1}\text{cm}^{-1}$ for 300 K agrees well with the published literature. Additionally σ_{opt} at the pseudogap lies below $\sigma_{opt}(\omega = 0)$ in the measured and published data. With the biggest gap in the measurement occurring between the 300 K and 200 K measurement which would suggest that the data below 300 K was scaled too low [35].

Sample 1050 shows some similarities in their optical conductivity with the as cast sample. Increasing the sample temperatures raises the intraband response in the optical conductivity for temperatures over 150 K, T > 150 K. Below 150 K the Drude transition seems to be temperature independent. Fitting the response reveals that the plasma scattering time, τ, tends to increase with higher temperatures. Temperature evolution of the plasma frequency, ω_p, indicates an initial decrease for raising temperatures up to 150 K and a slight increase for higher temperatures. The increasing of ω_p with higher temperatures (T > 150 K) could be responsible for the raised optical conductivity.

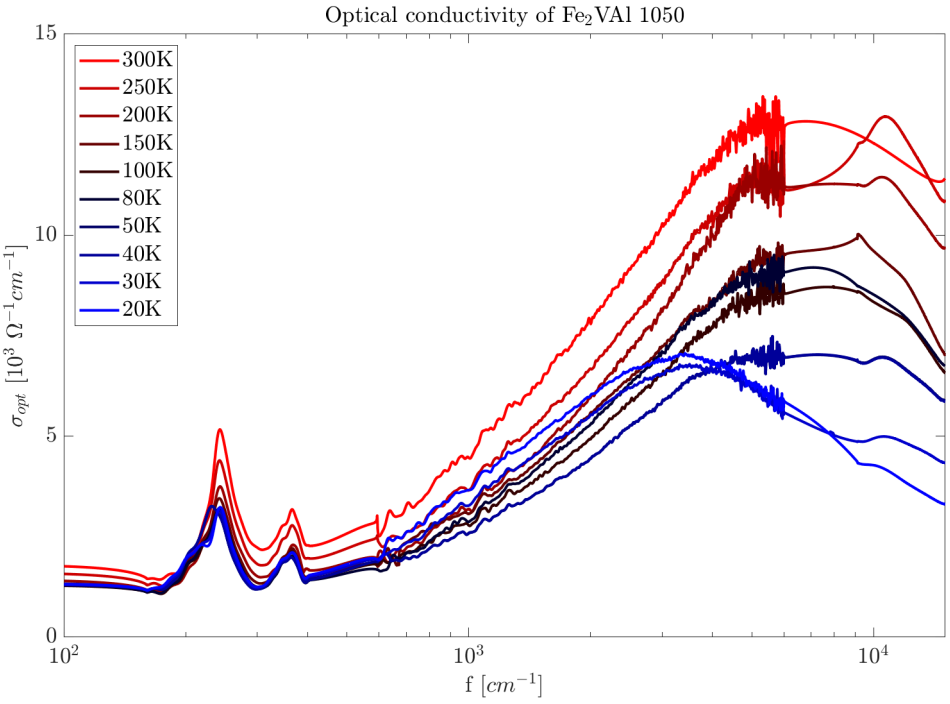

Figure 13: Optical Conductivity of Fe_2VAl 1050.

Similar to the as cast sample both optical phonons seem to decrease

with lower sample temperatures for T > 150 K. Below 150 K their intensity seems to be temperature independent. Modeling the response reveals that $\Delta\epsilon_1$ exhibits a minimum at 100 K and increases towards higher and lower temperatures. Additionally, the phonon damping, γ_1 decreases sharply with higher temperatures and stays fairly constant for temperatures over 100 K. Since the phononic response for T < 150 K lies in the region of measurement errors, it is difficult to confirm if its behavior is temperature independent in this domain. The fitting parameter ω_1 of the sample 1050 shows a decrease with lower temperatures which is opposite to the as cast sample. This might be a surprising effect, considering that through the dilation of the unit cell in the material with raising temperatures the phonon frequency should decrease [37].

Raising the sample temperature seems to intensify the interband transition. Very similar to the model for the as cast sample $\Delta\epsilon_3$ shows an increase in the interband transition with a higher temperatures.

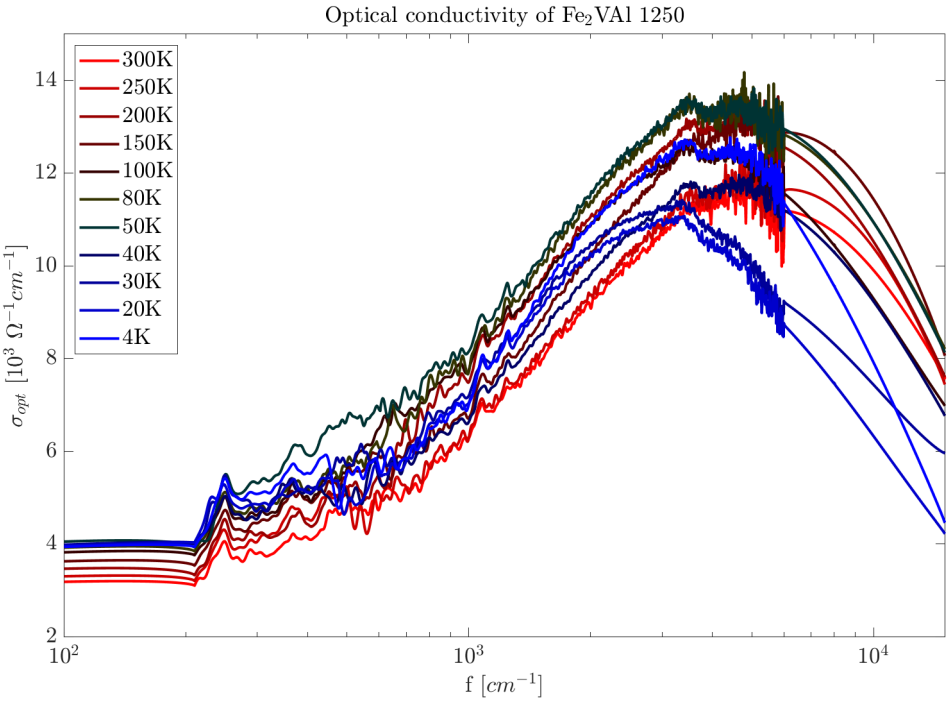

Figure 14: Optical Conductivity of Fe_2VAl 1250.

Optical conductivity measurements for the sample quenched at 1250 ° suggests that the response is much less dependent on the sample tem-

perature than for the as cast sample. It can be noted that the temperature dependence of the intraband transition seems to get stronger with lower sample temperature. The first phonon also seems to intensify with lower temperatures as well as the interband response. This is in stark contrast to the observed temperature dependence of the samples quenched at lower temperatures. Unfortunately, an accurate fitting was not possible for the temperature evolution of the sample 1250. Therefore, the behavior of some fitting parameters can only be guessed from the optical conductivity measurements. A slight shift to higher frequencies with lower temperatures can be observed in the maximum of the first phonon. As for the interband transition the maximum shifts towards lower frequencies for lower sample temperature. Additionally, it can be noted that a dip is visible in the interband transition which gets more pronounced for lower temperatures. This could be a possible sign that the interband transition is splitting.

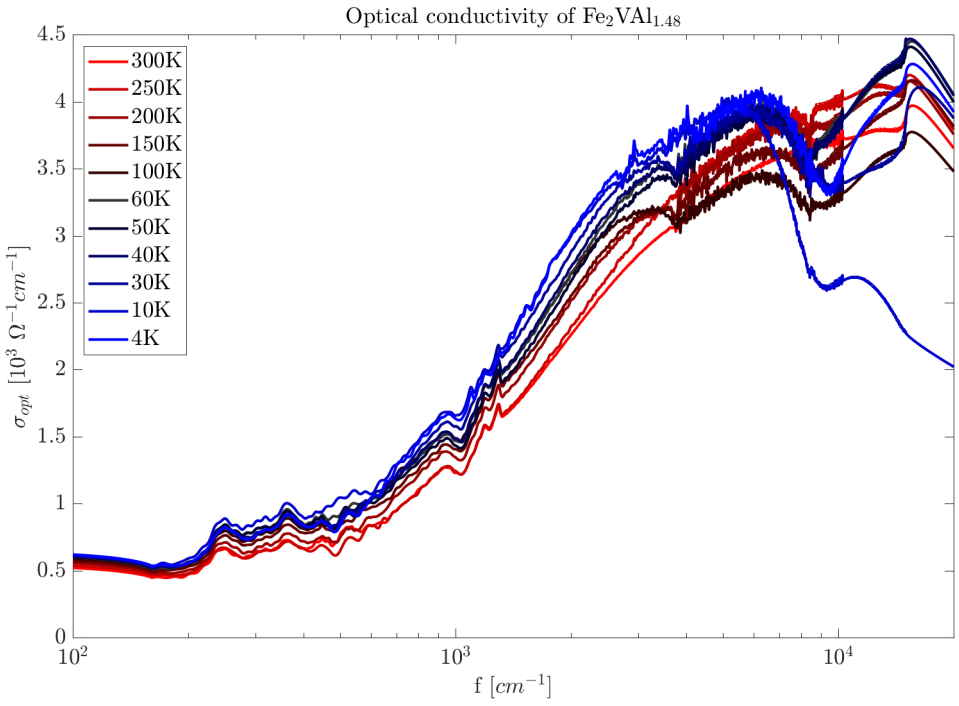

Figure 15: Optical Conductivity of $Fe_2VAl_{1.48}$ at different temperatures.

Lastly, the aluminum doped sample exhibits the least temperature dependence of all of the measured samples. The span of the temperature evolution of the intraband response almost completely lies in the range of the observed margin of error. It can be noted however, that

the Drude response seems to get stronger with lower temperatures, which is the opposite behavior observed in the as cast sample. Both phonons intensify with lowering temperature without a visible change in their overall shape. Decreasing the sample temperature seems to cause the interband response to grow. A visible dip in the interband transition could be an indication for the splitting of the interband response. Since, the measurement in this region was misaligned the pronounced dip might also be an artifact. Further measurements are required to classify the exact behavior of the interband response in this sample.

From the integration over the frequency of the optical conductivity in an interval from 0 to the cutoff frequency, ω_c, the spectral weights can be extracted according to the formula,

$$SW = \int_0^{\omega_c} \sigma_{opt}(\omega) d\omega. \tag{6.2}$$

A sum rule ensures that the integrated area under the optical conductivity stays unchanged at any temperature for a high enough cutoff frequency, ω_c. This means that the spectral weight is conserved for high enough frequencies [38].

A shift from low to high frequencies with raising quenching temperature can be seen in the spectral weigh, depicted in Figure 16 (a). The vanishing pseudogap is also detectable in the spectral weights as well as the evolution of the phonons. For a cutoff frequency of $\sim 10^4$ cm^{-1} the spectral weights for the samples at different quenching temperatures are very closed together. This might be a hint for the conservation of spectral weights at $\omega_c = 10^4$ cm^{-1} in samples with different quenching temperatures. However, it should be noted that the investigated frequency range was limited. As for the aluminum doped sample a redistribution seems to occur from higher to lower frequencies compared to the as cast sample. It should be noted that there remains a gap between the spectral weight of the as cast and the aluminum doped sample at $\omega_c = 10^4$ cm^{-1}.

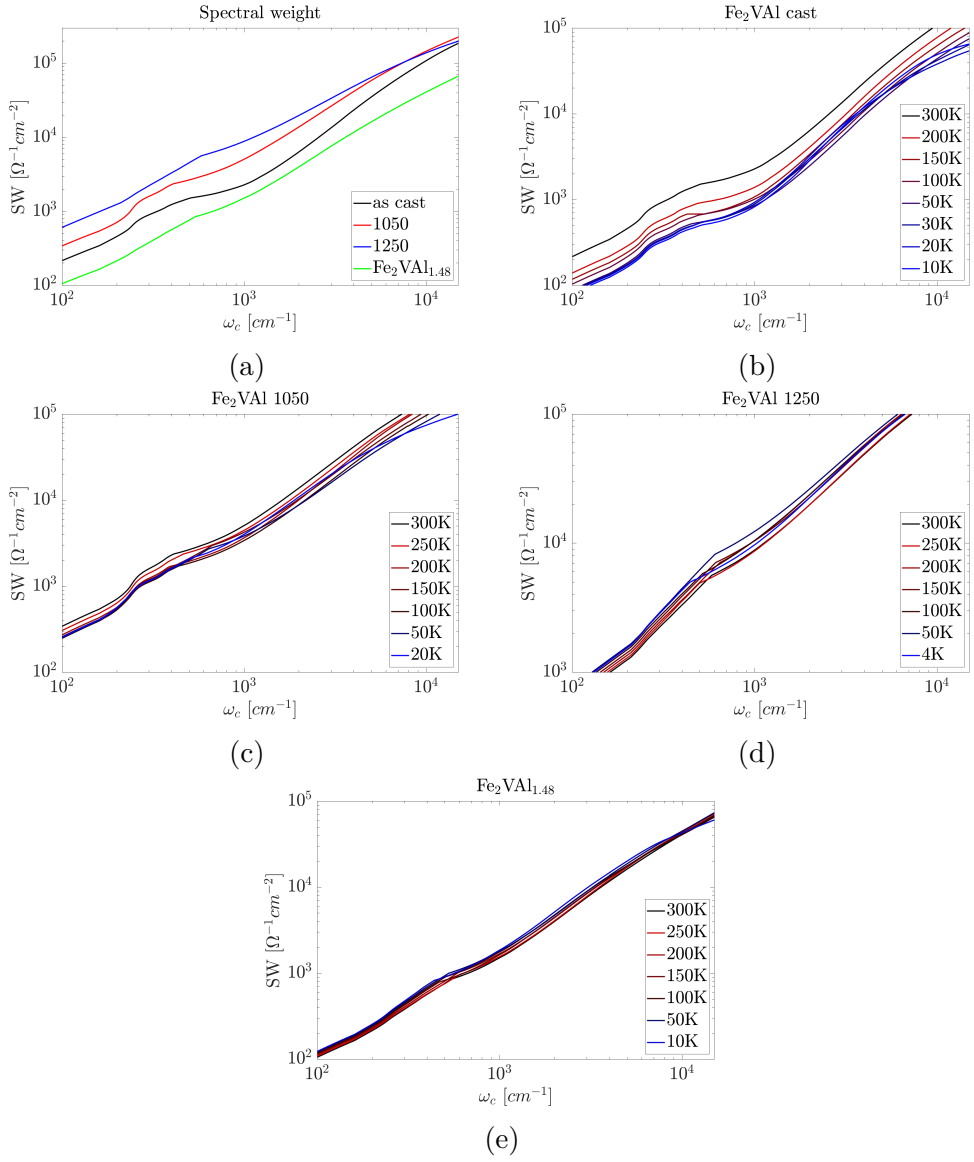

Figure 16: Calculated spectral weights for the investigated samples.

For the temperature evolution of a conventional semiconductor with an energy gap the Drude response vanishes with lower temperatures due to the loss of thermal excitation of the carriers. A vanishing Drude response was measured in the as cast and the 1050 sample with lowering sample temperature. This behavior is also visible in the spectral weights for the as cast and 1050 samples, which exhibit a shift towards lower frequencies with decreasing sample temperature.

It should be noted that the spectral weights for the as cast sample seems to not be conserved for a cutoff frequency of $\sim 10^4$ cm^{-1} with varying temperatures. This could be hint toward an incorrect

temperature-scaling of the data. Calculations for the sample 1050 at different temperatures seems to break the conservation of spectral weights, however less than the as cast sample. A diminished phononic response with decreasing temperatures can also be noted for the as cast and 1050 samples. Another noteworthy observation is the deviation of the spectral weights at higher frequencies for measurements below 50 K compared to the rest of them.

The fact that the 1250 and the Al-doped samples show little variation in their optical response over the studied temperature range also maps onto their calculated spectral weights. With spectral weights closely lying together for each of the sample at $\sim 10^4$ cm^{-1} over the investigated sample temperature range would suggest a conservation of spectral weights for this frequency range. The spectral weight is shifted to higher frequencies with decreasing sample temperature for the 1250 and the aluminum doped samples. Also their phononic response which intensifies at lower temperatures can be seen in their spectral weights.

7 Final remarks and outlook

The reflectivity measurements turned out to be challenging for multiple reasons. The small sample size restricted the accuracy of the data in far-infrared region. Larger sample sizes would therefore be useful in increasing the precision. Another issue being discovered was the errors due to the high reflectivity of the samples closely matching that of the reference. Gold depositioning of the samples in vacuum or the use of a microscope with a spectrometer would also be a useful investment for better measurements.

Electron-phonon interactions might be responsible for the difficulty in analyzing the observed optical phonons in the sample. Nevertheless, fitting the measurements showed less phonon damping with higher quenching temperatures. Which in turn would mean that the lifetime of the optical phonons are increased with higher quenching temperatures. This is an interesting result by itself because the thermal phonon conductivity is not affected. However, it is noteworthy that optical phonons do not contribute much to the thermoelectric transport.

On the other hand, the interband transition shows a clear shift towards lower frequencies with higher annealing temperatures and Al-doping. Due to the reduction of the interband transition in the optical data, the pseudogap in the density of states should also be decreased. This is a remarkable result which could hint at additional states appearing near the Fermi energy, E_F, in the density of states. Density functional theory calculations carried out for these systems showed hydrogen-like impurity states near E_F in the density of states. Although, the pseudogap in the density of states could not be measured directly, the emergence of impurity states could explain the observed reduction in the frequency of the interband transition. This is a remarkable result by itself and could explain the increased ZT value for the disordered materials.

Further research is needed to confirm the exact evolution of the pseudogap and to confirm the existence of impurity states appearing near E_F. Nevertheless, from the optical data a plausible progression of the density of states can be drawn under the assumption that the band

structure is rigid for the growing disordered lattice system. In such a case quenching with higher temperatures would introduce an impurity state near E_F. With growing antisite disorder in the lattice system the impurity state would get stronger and resembles a Dirac-like distribution more closely. A schematic drawing of this can be seen in Figure 17. With the theoretical knowledge laid out in this work above, such a scenario would increase the thermoelectric figure of merit for higher quenching temperatures. Sample $Fe_2VAl_{1.48}$ would also show a similar impurity state emerging which was suggested by performed density functional theory calculations [29, 30].

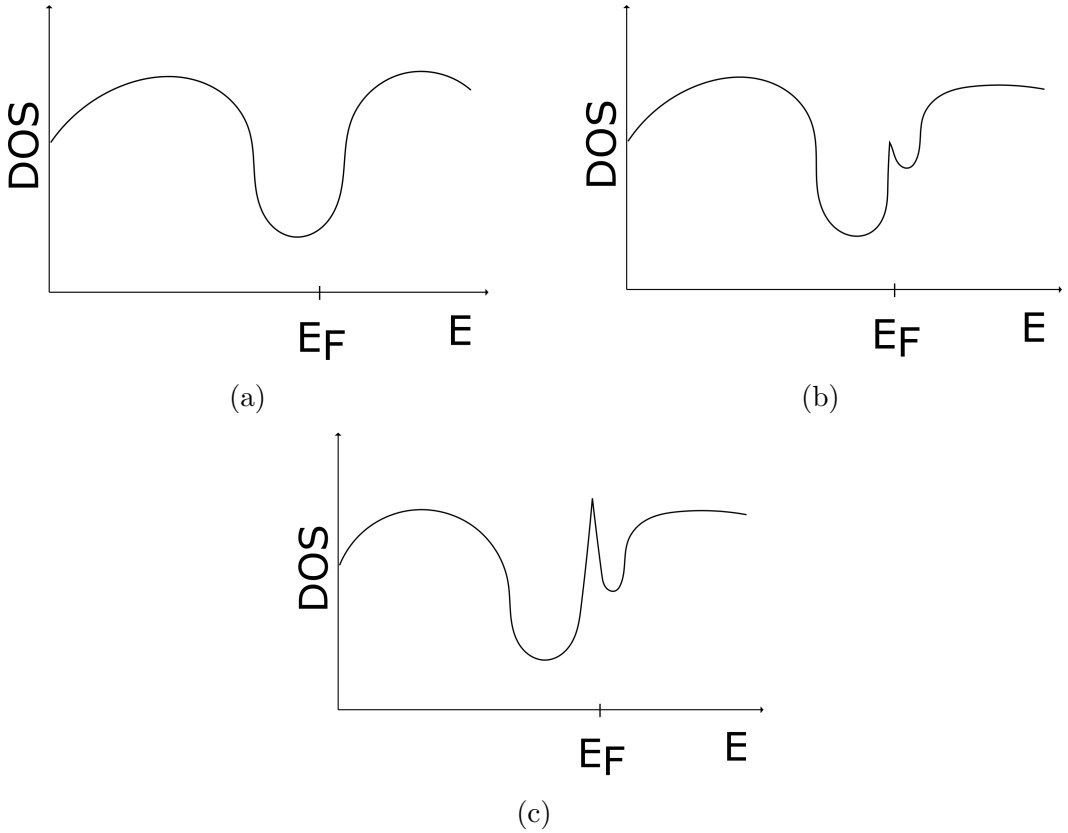

Figure 17: Hypothetical schematic drawing of the evolution of the impurity state in the density of states (DOS) near E_F. With increasing annealing temperture, low annealing (a) to high annealing temperture (c), the impurity state becomes more prounounced.

Quenching the system had also a notable effect on the interband transition and the optical conductivity. Measurements indicated that the interband response moves to lower frequencies with increasing quenching temperature. An increase in the optical conductivity with raising

quenching temperature was also measured which could be beneficial for the ZT value.

Captured measurements over the investigated sample temperature range showed little alterations in the optical conductivity. This could be beneficial for the thermal stability of the thermoelectric figure of merit. The fitting process turned out to be more challenging then thought and it was not possible to fit the 1250 and the aluminum doped samples to a sufficient degree of satisfaction. Some fitting parameters showed inconsistencies with previously published results as for the carrier contraction. The temperature evolution of parameters like the plasma frequency, ω_p, might be improved by further investigation.

All in all, further research is needed in order to improve the optical conductivity measurements. Certain deviation from literature and the conducted measurements in this work might be resolved by improving the measurement technique with which the evolution of the diminished pseudogap could be quantified.

8 Acknowledgments

This endeavor would not have been possible without long discussions and help by Evan Constable.

I would also like to thank Andrei Pimenov for the opportunity to write this thesis and for his feedback to my progress.

I'm extremely grateful to Fabian Garmroudi and Michael Parzer for providing me with their samples and their fruitful input to my work.

Lastly I wanna thank my family, my friends and all the people who helped me.

References

[1] UN, "Transforming our world: the 2030 agenda for sustainable development," 2015. [Accessed October 24, 2022].

[2] H.-O. Pörtner, D. C. Roberts, M. M. B. Tignor, E. Poloczanska, K. Mintenbeck, A. Alegría, M. Craig, S. Langsdorf, S. Löschke, V. Möller, A. Okem, and B. Rama, "Climate change 2022: Impacts, adaptation and vulnerability," *IPCC Sixth Assessment Report*, 2022.

[3] A. Bharwdaj, K. S. Jat, S. Patnaik, Y. N. Parkhomenko, Y. Nishino, and V. V. Khovaylo, "Current Research and Future Prospective of Iron-Based Heusler Alloys as Thermoelectric Materials," vol. 14, pp. 281–289, 2019.

[4] S. Twaha, J. Zhu, Y. Yan, and B. Li, "A comprehensive review of thermoelectric technology: Materials, applications, modelling and performance improvement," vol. 65, pp. 698–726, 2016.

[5] M. Mikami, Y. Kinemuchi, K. Ozaki, Y. Terazawa, and T. Takeuchi, "Thermoelectric properties of tungsten-substituted heusler Fe_2VAl alloy," vol. 111, 2012.

[6] B. Hinterleitner, I. Knapp, M. Poneder, Y. Shi, H. Müller, G. Eguchi, C. Eisenmenger-Sittner, M. Stöger-Pollach, Y. Kakefuda, N. Kawamoto, Q. Guo, T. Baba, T. Mori, S. Ullah, X.-Q. Chen, and E. Bauer, "Thermoelectric performance of a metastable thin-film Heusler alloy," vol. 576, pp. 85–90, 2019.

[7] K. Rupp, *Numerical solution of the Boltzmann transport equation using spherical harmonics expansions.* PhD thesis, 2009.

[8] A. H. Wilson, "The theory of metals," *The Theory of Metals*, 2011.

[9] A. Kumar, S. Bano, B. Govind, A. Bhardwaj, K. Bhatt, and D. K. Misra, "A Review on Fundamentals, Design and Optimization to High ZT of Thermoelectric Materials for Application to Thermoelectric Technology," vol. 50, 2021.

[10] H. Lee, *Thermoelectrics: design and materials.* John Wiley & Sons, 2016.

[11] G. Chen, M. Dresselhaus, G. Dresselhaus, J.-P. Fleurial, and T. Caillat, "Recent developments in thermoelectric materials," *International materials reviews*, vol. 48, pp. 45–66, 2003.

[12] A. Bulusu and D. Walker, "Review of electronic transport models for thermoelectric materials," vol. 44, pp. 1–36, 2008.

[13] M. Kinza, *Theorie der Fermiflüssigkeit in Metallen: Ein kompakter Überblick als Einführung in die Theoretische Festkörperphysik.* essentials, Springer Fachmedien Wiesbaden, 2018.

[14] A. F. Ioffe, L. Stil'Bans, E. Iordanishvili, T. Stavitskaya, A. Gelbtuch, and G. Vineyard, *Semiconductor thermoelements and thermoelectric cooling.* Infosearch, ltd., London, 1957.

[15] C. Hapenciuc, T. Borca-Tasciuc, and I. Mihailescu, "The relationship between the thermoelectric generator efficiency and the device engineering figure of merit $Z_{d,eng}$. The maximum efficiency η_{max}," *AIP Advances*, vol. 7, 2017.

[16] G. S. Nolas, J. Sharp, and J. Goldsmid, *Thermoelectrics: basic principles and new materials developments*, vol. 45. Springer Science & Business Media, 2013.

[17] M. Hamid Elsheikh, D. A. Shnawah, M. F. M. Sabri, S. B. M. Said, M. Haji Hassan, M. B. Ali Bashir, and M. Mohamad, "A review on thermoelectric renewable energy: Principle parameters that affect their performance," vol. 30, pp. 337–355, 2014.

[18] G. J. Snyder and E. S. Toberer, "Complex thermoelectric materials," in *Materials for sustainable energy: a collection of peer-reviewed research and review articles from Nature Publishing Group*, pp. 101–110, World Scientific, 2011.

[19] X. Zhang and L.-D. Zhao, "Thermoelectric materials: Energy conversion between heat and electricity," *Journal of Materiomics*, vol. 1, pp. 92–105, 2015.

[20] T. Zhu, Y. Liu, C. Fu, J. P. Heremans, J. G. Snyder, and X. Zhao, "Compromise and synergy in high-efficiency thermoelectric materials," *Advanced materials*, vol. 29, 2017.

[21] J. He, M. G. Kanatzidis, and V. P. Dravid, "High performance bulk thermoelectrics via a panoscopic approach," vol. 16, pp. 166–176, 2013.

[22] H. J. Goldsmid *et al.*, *Introduction to thermoelectricity*, vol. 121. Springer, 2010.

[23] F. Wooten, "Optical properties of solids," *American Journal of Physics*, vol. 41, no. 7, pp. 939–940, 1973.

[24] D. Narducci, E. Selezneva, G. Cerofolini, S. Frabboni, and G. Ottaviani, "Impact of energy filtering and carrier localization on the thermoelectric properties of granular semiconductors," vol. 193, pp. 19–25, 2012.

[25] S. Hooshmand Zaferani, R. Ghomashchi, and D. Vashaee, "Strategies for engineering phonon transport in Heusler thermoelectric compounds," vol. 112, pp. 158–169, 2019.

[26] G. Mahan and J. Sofo, "The best thermoelectric," *Proceedings of the National Academy of Sciences*, vol. 93, pp. 7436–7439, 1996.

[27] T. Graf, C. Felser, and S. S. Parkin, "Simple rules for the understanding of Heusler compounds," vol. 39, pp. 1–50, 2011.

[28] S. Bandaru, A. Katre, J. Carrete, N. Mingo, and P. Jund, "Influence of Antisite Defects on the Thermoelectric Properties of Fe $_2$ VAl," vol. 21, pp. 237–246, 2017.

[29] F. Garmroudi, M. Parzer, A. Riss, A. Ruban, S. Khmelevskyi, M. Reticcioli, M. Knopf, H. Michor, A. Pustogow, T. Mori, and E. Bauer, "Anderson transition: A novel route to high thermoelectric performance," 2021.

[30] M. Parzer, F. Garmroudi, A. Riss, S. Khmelevskyi, T. Mori, and E. Bauer, "High solubility of Al and enhanced thermoelectric performance due to resonant states in Fe_2VAl_x," vol. 120, 2022.

[31] W. Demtröder, *Experimentalphysik 2*. Springer, Kaiserslautern, 2013.

[32] P. R. Griffiths and J. A. De Haseth, *Fourier transform infrared spectrometry*. John Wiley & Sons, 2007.

[33] Bruker, "VERTEXseries Brochure EN." `https://www.bruker.com/fileadmin/user_upload/8-PDF-Docs/OpticalSpectrospcopy/FT-IR/VERTEX/Brochures/VERTEXseries_Brochure_EN.pdf`, 2018. [Accessed November 22, 2020].

[34] S. S. Ng, Z. Hassan, and H. Abu Hassan, "Kramers–Kronig Analysis Of Infrared Reflectance Spectra With A Single Resonance," vol. 44, pp. 67–76, 2006.

[35] H. Okamura, J. Kawahara, T. Nanba, S. Kimura, K. Soda, U. Mizutani, Y. Nishino, M. Kato, I. Shimoyama, H. Miura, K. Fukui, K. Nakagawa, H. Nakagawa, and T. Kinoshita, "Pseudogap formation in the intermetallic compounds $(Fe_{1-x}V_x)_3Al$," vol. 84, pp. 3674–3677, 2000.

[36] Y. Feng, J. Y. Rhee, T. A. Wiener, D. W. Lynch, B. E. Hubbard, A. J. Sievers, D. L. Schlagel, T. A. Lograsso, and L. L. Miller, "Physical properties of heusler-like Fe_2VAl," vol. 63, p. 165109, 2001.

[37] R. Schleck, R. Moreira, H. Sakata, and R. Lobo, "Infrared reflectivity of the phonon spectra in multiferroic TbMnO 3," *Physical Review B*, vol. 82, no. 14, p. 144309, 2010.

[38] A. Perucchi, L. Degiorgi, R. Hu, C. Petrovic, and V. F. Mitrović, "Optical investigation of the metal-insulator transition in FeSb2," vol. 54, pp. 175–183, 2006.